TÍTULO

SOLUBILITY AND DISSOCIATION OF IONIC LIQUIDS IN EPOXIDES AND CYCLIC CARBONATES BY MOLECULAR DYNAMICS

AUTOR

Sergio Dorado Alfaro

Esta edición electrónica ha sido realizada en 2025

Director	Dr. Felipe Jiménez Blas
Institución	Universidad Internacional de Andalucía
Curso	*Máster Universitario en Simulación Molecular (2023/24)*
©	Sergio Dorado Alfaro
©	De esta edición: Universidad Internacional de Andalucía
Fecha documento	2024

Universidad Internacional de Andalucía
Máster en Simulación Molecular

SOLUBILITY AND DISSOCIATION OF IONIC LIQUIDS IN EPOXIDES AND CYCLIC CARBONATES BY MOLECULAR DYNAMICS

Sergio Dorado Alfaro
Trabajo de Fin de Máster

Director: Felipe Jiménez Blas
Co-Director: José Francisco Palomar Herrero

Curso Académico: 2023/2024
Madrid, julio 2024

"How wonderful that we have met with a paradox.
Now we have some hope of making progress."
Niels Bohr

INDEX

ABSTRACT

Climate emergency has led to the investigation of CO_2 valorisation routes capable of converting this greenhouse gas into a valuable resource. A competitive process included in this circular economy transition framework is the catalytic CO_2 cycloaddition to epoxides, to produce cyclic carbonates. Halide-based Ionic liquids have been postulated to be a competitive choice to catalyse this reaction by their favourable physico-chemical properties, which can be enhanced towards specific objectives by cation and anion selection and functionalization. In this context of improvement, experimental and DFT theoretical studies have been carried out, leading to inconsistencies and contradictions regarding the cations and anions effects, resulting impossible until recently to set generalizations that permit the construction of an effective route for molecule design towards the optimization of the catalytic activity in terms of the carbonate yield. Latest studies have found that cation-anion dissociation constant is a key descriptor of the catalytic activity and is intimately linked to the cation-anion interaction strength. It has been found that cation-anion interaction is predominant, confirmed experimentally by low conductivities of the epoxide medium with dissolved Ionic Liquid. This result has led to question the most extended paradigm that considers ionic liquids ions as dissociated free interacting species, which is the fundament of the most extended reaction mechanism. In this work, the problem was addressed by a different simulation technique, classical molecular dynamics. To replicate experimental conditions, propylene epoxide and carbonate force fields found in the literature were evaluated in terms of their vapor-liquid phase equilibria. With the epoxide and carbonate ready and with CL&P force field model for ionic liquids, solubilities were tested for [N4444] and [N2222] cations combined independently with the halide anions [I], [Br] and [Cl]. Results showed that [N2222] cation-based ionic liquids crystalized and were therefore insoluble in the epoxide/carbonate medium, whereas [N4444] cation-based ionic liquids demonstrated slow diffusion. Both results were endorsed experimentally. Simulation visualizations showed ion pairs rather than dissociation species. Lastly, reaction medium interactions were studied between key atoms in terms of the reaction mechanism. It was found that cation-anion interaction follows the catalytic activity trend, being [I] the halide anion less associated with the three studied cations ([N4444], [bmim] and [emim]), and at the same time, being those ionic liquids the ones that displayed a better interaction between the cation and the epoxide Oxygen, phenomena that can be liked to epoxide activation and reaction intermediates stabilization. Therefore, the path towards the understanding of the mechanisms underlying the catalytic activity has been widen, with new simulation techniques that have enabled a better understanding of the complex interactions interplay present in this catalytic system.

1. INTRODUCTION

Since the onset of the industrial revolution, human activities have significantly contributed to greenhouse gas emissions, principally due to fossil fuels burning for energy production. This steady increase in global concentrations of carbon dioxide (CO_2) (**Fig. 1a**) and methane, which is made patent by global reports, has been strongly correlated to environmental changes, generally referred as climate change consequences. Examples of these environmental changes are rising temperatures (**Fig.1b**), rising sea levels (**Fig.1b**) and oceans acidification. These changes not only damage terrestrial, ocean and freshwater ecosystems, but also significantly impact human societies through natural disasters intensification, mental health diminution and malnutrition, as stated by IPCC reports **[1-4]**.

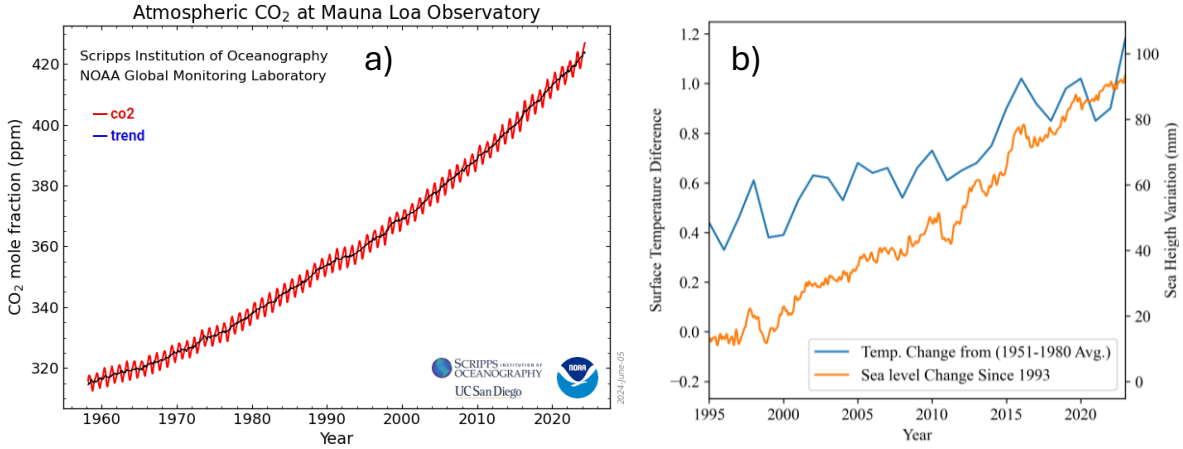

Figure 1. a) Global CO_2 concentration increase since 1960. b) Global temperature increase relative to the long term average between 1951 and 1980 (blue) and sea level variation relative to 1993 (orange), both since 1995.

Social concern over climate change has prompted developed countries governments to formulate global commitment plans that limit global warming to 1.5ºC by gas emissions reductions, aiming net-zero by 2050 **[5]**. This ambitious goal would be achieved by the development of clean energy sources as a long-term solution, coupled with the technological development and operation of Carbon Capture and Utilization (CCU) and Carbon Capture and Storage (CCS) plants, which serve as both short- and long-term solutions. CCUS are present in new energetic carrier development like biogas, which needs an upgrading process for quality standards compliance, on-site carbon capture and very importantly carbon capture delocalization, which can result in net-zero or negative carbon emissions by performing direct air capture (DAC) away from the carbon source. Thus, there is a need to convert CO_2 into a resource rather than consider it a pollutant, process in which CCU plants become essential as a mitigation technique in the environmental transition framework towards more sustainable societies based on a circular economy **[6, 7]**.

Obtaining a valuable product from CO_2 is therefore crucial to achieve the economic success of CCU processes, being cyclic carbonates and polycarbonates a strong and frequently investigated approach in the literature **[8-10]**. These compounds can be synthesized by the CO_2 cycloaddition to epoxides, in a reaction that achieves 100% atom efficiency **[10,11]**. Reaction routes capable of synthesizing cyclic carbonates or

derivates from it can be seen in **Fig. 2** along with market size estimates of the obtainable products **[10]**.

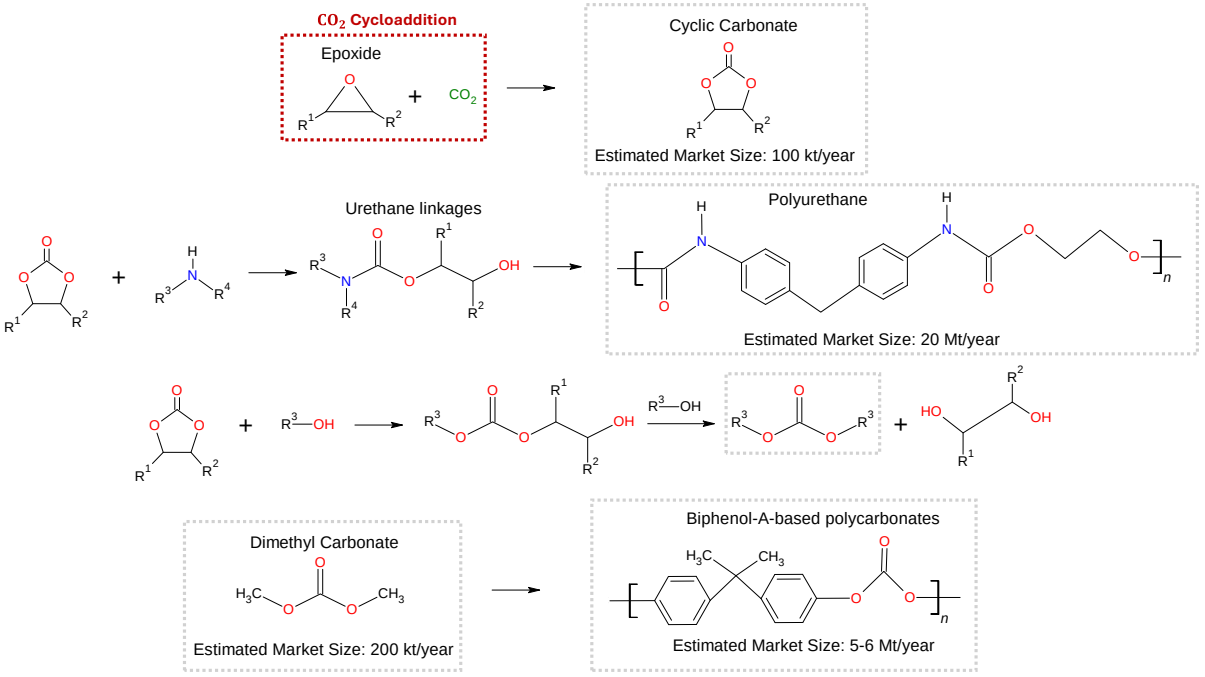

Figure 2. Product examples of polymers and fine chemicals along with their estimated market size which can be obtained from or as derivatives of CO_2 cycloaddition to epoxides reaction. Adapted from **[10]**.

Among the most important applications of cyclic carbonates are their use as electrolytes for lithium-based batteries, in paint stripping, coatings and lubricants, along in the synthesis of derivate chemicals like polyurethane (**Fig. 2**) **[12-15]**. Cyclic carbonates can also be used as green solvents in membrane separation or simply in separation stages in classical hydrocarbon separations and in pharmaceutical extractions from water as useful hydrophobic solvents **[16-20]**. Lastly, cyclic carbonates can be used for polycarbonates production by means of the Ashi Kasei non-phosgene process (last two lines in **Fig. 2**) with flexibility on the incorporated chemical groups **[10]**, which expands their applicability to fields like medicine. Therefore, CO_2 cycloaddition to epoxides constitutes a promising route for CO_2 valorisation whose optimization and addressing of challenges are mandatory to achieve competitiveness with the less sustainable conventional routes capable of synthesizing the same products.

An important aspect of CO_2 cycloaddition to epoxides is the need of homogeneous or heterogeneous catalysts **[13]**. The catalyst selection affects the product obtained. Cyclic carbonates are usually obtained when using Lewis bases without a Lewis acid, like halide salts or halide-based Ionic Liquids (ILs), or Lewis acids combined with bases without the presence of metals. Alternatively, the combination of Lewis acids and bases containing metals tend to form polycarbonates, even though metal catalysts present disadvantages such as their elevated cost, toxicity and low chemical stability **[10, 21, 22]**. Metal-free catalysts like ILs are promising for their negligible vapour pressure, adequate thermal stability and very importantly, they offer a vast tunability by cation and anion change and functionalization, enabling chemical structure design for specific purposes and applications as aforementioned catalytic step **[23-25]**. Additionally, ILs

can offer both physical and chemical CO_2 capture, which enables their applicability at lowest CO_2 partial pressures conditions through the so-called integrated CCU concept **[26]**. All these advantages have led to their characterization by both experimental and computational techniques, in which different cations and anions combinations have been tried. Most common cations correspond to imidazolium-, ammonium-, phosphonium-, pyridinium and bis(triphenylphosphine)iminium-based groups **[10, 22, 27]**, being first two the groups that will be studied in this work. In terms of the anion, halides are the most extended, especially [Cl] and [Br], being [I] incorporated in the latest research experiments **[27-29]**.

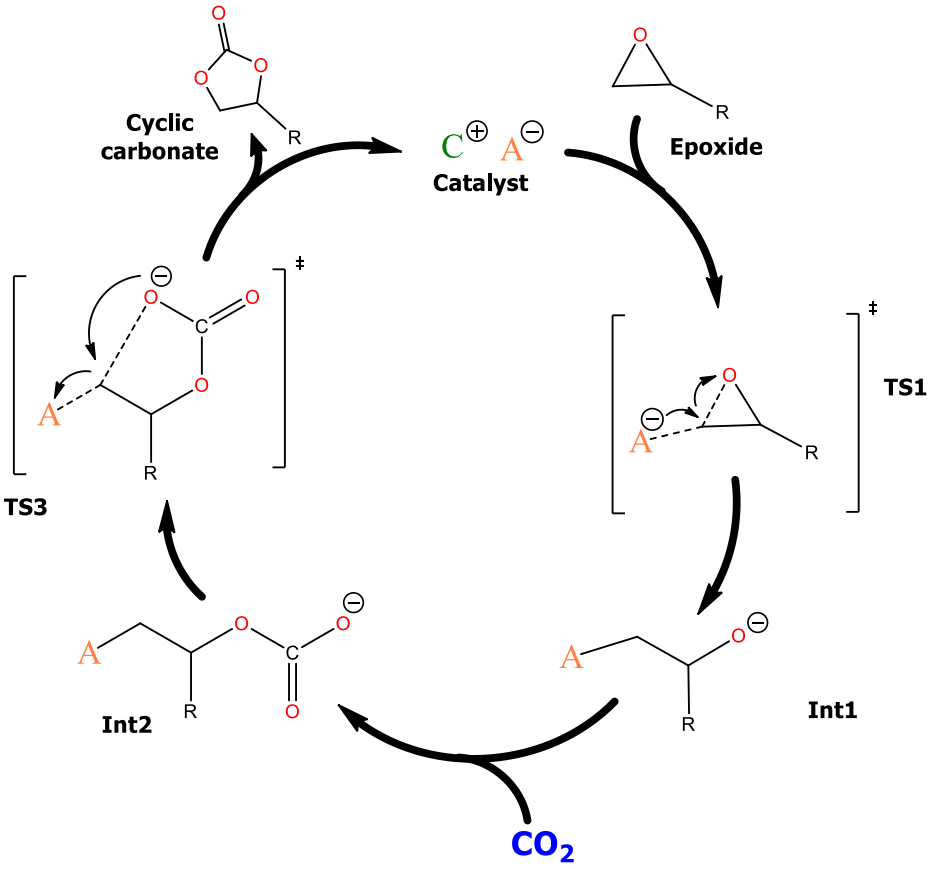

Figure 3. Most extended reaction mechanism of CO_2 cycloaddition to epoxides by Ionic Liquids catalysts. Reproduced with permission from **[29]**.

Several reaction mechanisms have been attributed to CO_2 cycloaddition to epoxides by halide-based ILs catalysts. The most accepted one is depicted in **Fig. 3**. This mechanism starts with the opening of the epoxide ring by the nucleophilic attack of the halide anion, forming an intermediate specie (**Int1**) in which the anion is covalently bonded. In the next step, **Int1** captures CO_2 and adds it to the chain, displacing the negative charge and forming a new intermediate (**Int2**). Finally, intramolecular cyclization occurs, forming the cyclic carbonate and regenerating the catalyst by expulsing the anion back into the reaction medium **[9, 10, 13, 21, 22, 30-34]**. Additionally, it has been proposed that the cation due to its acidic nature first interacts with the oxygen of the epoxide by hydrogen bonding, therefore activating the epoxide for reaction and empowering the nucleophilic attack, serving as an intermediate stabilator afterwards **[30, 35-38]**. This variation is depicted in **Fig. 4** and has been

proposed for catalysts composed a Lewis Acid (LA) and a Lewis Base (LB) **[10]**. One aspect that supports this hypothesis for the cation influence is that the use of hydrogen bond donor's solvents capable of interacting with the epoxide has been demonstrated to improve the reaction **[22, 38, 40, 41]**.

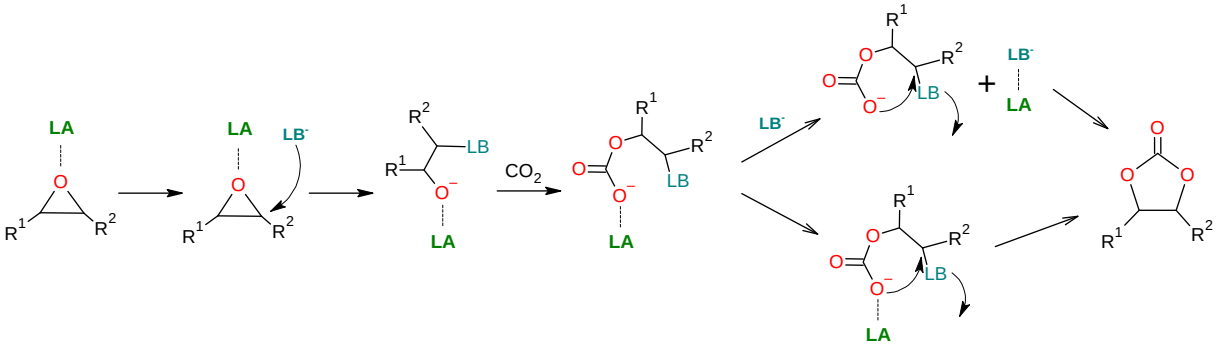

Figure 4. Reaction mechanism for a catalyst composed of a Lewis Base (LB) and a Lewis Acid (LA). LA activates the epoxide by interacting with the oxygen. In the following steps the Lewis Acid stabilises the intermediates until the carbonate formation **[10]**.

The catalytic activity of halide-based ILs has been a topic of great discussion in the literature, being the absence of systematic and comparable experiments until the latest studies **[29]** one of the causes that has impeded the understanding of the ions effect, resulting in some controversy on the matter. The most common experimental trend in terms of the anion finds that the catalytic performance follows the inverse order to the nucleophilic character of the anions in an aprotic medium: [I] > [Br] > [Cl] **[22, 41, 42]**. This order is the opposite to the one expected by DFT calculations **[29]**, which finds that for intermediates with [I], intermediates are the most energetic in comparison to [Br] and [Cl] as shown in **Fig.5**.

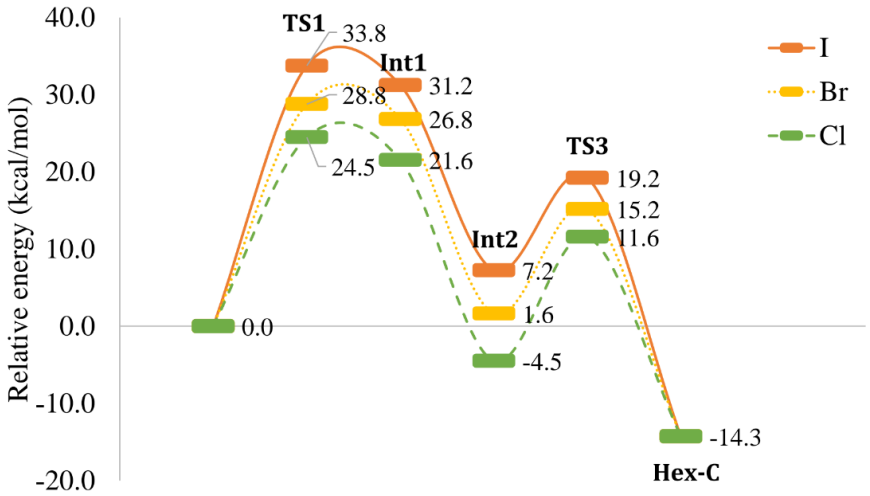

Figure 5. Relative energies found from DFT calculations performed over of the different reaction species of the most extended mechanism in the CO_2 cycloaddition to epoxides by halide-based Ionic Liquids. Reproduced with permission from **[29]**.

This discrepancy has been partially explained by the leaving ability of the anions, which follows the experimental catalytic performance trend and would play a significant role in the **TS3** step of the reaction mechanism depicted in **Fig. 3 [34, 42]**. DFT calculations do not agree with this conclusion, since the energy barrier between intermediate **Int2**

to cyclic carbonate product (**TS3**) is higher in [I] than in [Br] and [Cl] (**Fig.5**). Nevertheless, other studies find better catalytic activities with [Br] along with trend changes for different cations **[30, 34, 41, 42]**. Therefore, the catalytic activity is thought to be influenced by both anion nucleophilicity, in charge of the epoxide ring opening, and the leaving ability, for the carbonate formation, which can in fact be determined not only by the anion but also with great influence of the cation, the epoxide used as reactant and the reaction medium **[43]**. For the systems in which anion influence is studied in this work, catalytic activity follows the experimental trend [I] > [Br] > [Cl] for [N4444], [bmim], and [emim] cations, while the inverse order is found for [N2222]-based ILs which are not soluble in the epoxide **[29]**, as depicted in **Fig. 6a** with more detail in solubilities and yield values.

In terms of the cation, their versatility has led to very different interpretations yet without an agreement on how they affect the catalytic activity. What is known for sure, is that cation severely affects the catalytic activity, given that latest systematic experimental studies find that by keeping the anion fixed while trying for different cations, epoxide conversion varies in almost the whole possible spectra **[29]**. This behaviour can be seen in **Fig. 6b** for [Br] anion combined with different cations. It can be noted that yields vary from 76% for [N4444] cation to 0% for [N1111] cation, being both completely soluble in the epoxide medium. Some authors suggest that longer chain lengths improve catalytic activity **[37, 44, 45]**, while others find the opposite and attribute the variability to the catalyst acidity **[42]**, therefore a definitive explanation remains absent. Solubility in the epoxide is in fact another determinant property of these catalysts, that greatly depends on the cation selection **[46]**. Given that the epoxide is the solvent and at the same time a reactive specie, solubility changes over the reaction course, generally improving the catalyst solubility because of the greater polarity of the cyclic carbonates formed **[47]**.

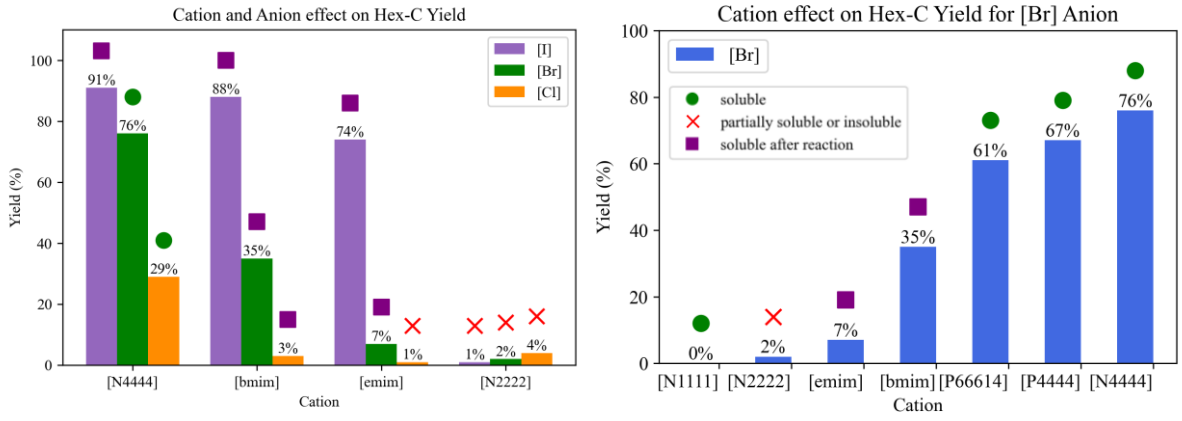

Figure 6. Cation and Anion effect over experimental yields and solubilities for different cation and anion combinations. Solubility expressed by symbols on top of the bars and is conserved between plots. Experimental data taken from **[29]**

DFT studies have been carried out aiming to explain the experimental results. Nevertheless, contradictions have also emerged concerning both the cation and the anion role **[23, 31, 35, 48, 49]**. A cooperative action between halide anions and imidazolium cations has been proposed to explain [emim][Cl] **[35]** and [bmim][Br] **[48]** catalytic activity, suggesting that cations might be able to stabilize the reaction intermediates and the transition states, promoting anion nucleophilic attack **[31, 34]**.

Other calculations propose that these anion activities significantly depend on the cation and solvents, in which a balance between the nucleophilic character of the anion (in charge of epoxide ring opening) and the cation-anion interaction (also favoured) should be achieved **[30]**. In terms of the cation's substituents, hydrogen bond donor groups show reduced energy barriers by DFT calculations **[33, 35, 48]**, but experimental catalytic activity performed with cations containing hydroxyl groups is reduced **[33]**. Other DFT studies cantered in the alkyl chain lengths show the same energy barriers for different chain lengths **[35]**. This is once again in contradiction with experimental results that show greater yields for cations with longer side chains. Alternative studies based on DFT/COSMO-RS approaches were successfully used for cation-anion interaction description through the IL dissociation equilibrium constant (K_D) calculation **[29,50]**, which has been experimentally validated (**Fig. 7b**) by the dissociation degree (ξ), obtained from experimental results of conductivity (λ) at 65ºC in the epoxide and dissolved IL catalysts. K_D is to date the most successful approach for catalytic activity description, achieving from a logarithmic regression between carbonate yield and K_D of the ILs that will be studied in this work an R^2 of 0.81, as demonstrated in **Fig. 7a**. Yield, λ, ξ and K_D data attributed for each IL catalyst can be found in **Table 1 [29]**.

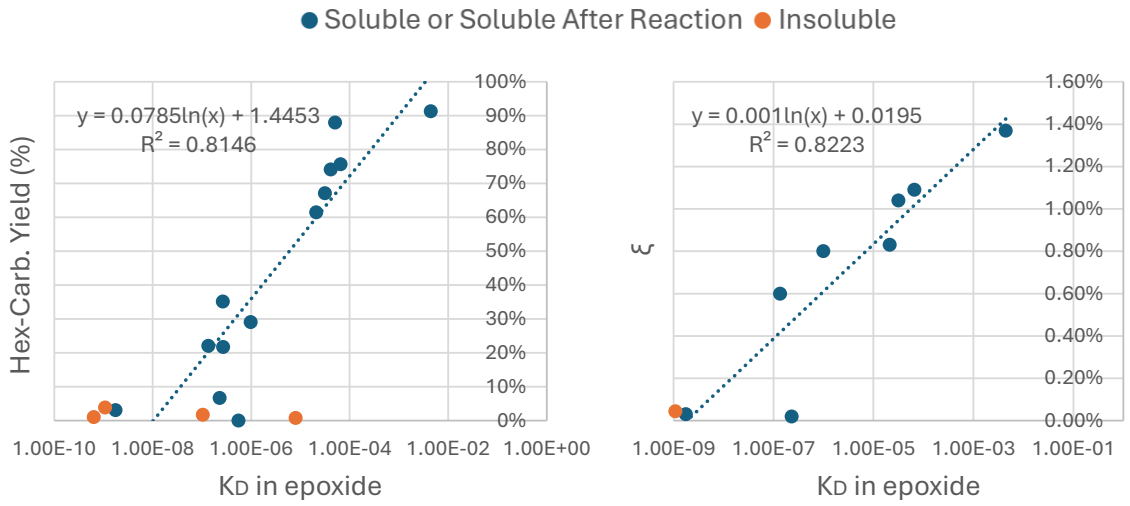

Figure 7. Experimental hexylene carbonate yield against dissociation equilibrium constant (K_D) for soluble (blue) and insoluble (orange) halide-based Ionic Liquids catalysts. Regression performed exclusively on soluble ones. Data taken from **[29]**.

The discrepancies found between DFT calculations and experimental results, along with the success of K_D constant is probably due to the inability of DFT calculations to consider bulk properties such as solubility, solvation and, transport phenomena. Calculated K_D values are in fact much lower than expected initially, but the experimental confirmation came afterward **[29]**. This result is crucial, given that low conductivities also mean low dissociation of the ionic liquids catalysts, which means that ions are not dissociated and freely moving through the reaction medium, as it would be expected by the reaction mechanism. Therefore, most recent studies propose that these ILs catalysts are distributed in the form of aggregates rather than in a homogeneous dissociated phase **[29]**, vision that is inaccessible by DFT calculations where isolated or a very reduced number of molecules are present. All these results open an interesting debate:

How can dissociated ions be considered the active species in the reaction mechanism if the experimental measurements find strong ion interactions and therefore very low dissociation degrees?

Table 1. Experimental ionization and dissociation constant calculated with COSMO-RS. Data taken from **[29]**.

IL	Yield Hex	Solubility	λ at 65ºC (S/m)	ξ	KD
[P66614][Br]	61%	S	8.77E-03	0.83%	2.10E-05
[N4444][Br]	76%	S	1.18E-02	1.09%	6.56E-05
[P4444][Br]	67%	S	1.12E-02	1.04%	3.14E-05
[N4444][Cl]	29%	S	8.97E-03	0.80%	9.79E-07
[P66614][Cl]	22%	S	6.56E-03	0.60%	1.35E-07
[P4444][Cl]	22%	S	-	-	2.69E-07
[N1111][Br]	0%	S	-	-	5.55E-07
[N4444][I]	91%	SAR	1.42E-02	1.37%	4.41E-03
[bmim][I]	88%	SAR	-	-	5.05E-05
[emim][I]	74%	SAR	-	-	4.13E-05
[bmim][Br]	35%	SAR	-	-	2.66E-07
[emim][Br]	7%	SAR	2.20E-04	0.02%	2.29E-07
[bmim][Cl]	3%	SAR	3.90E-04	0.03%	1.75E-09
[N2222][Cl]	4%	IN	4.48E-04	0.04%	1.08E-09
[N2222][Br]	2%	IN	-	-	1.04E-07
[emim][Cl]	1%	IN	-	-	6.33E-10
[N2222][I]	1%	IN	-	-	7.98E-06

S: Soluble, SAR: Soluble After Reaction, IN: Insoluble

Answering this question constitutes the principal motivation of this work, in which an alternative molecular simulation method is tried: Classical Molecular Dynamics. This simulation method allows the analysis of the reaction medium, covering the inspection of the interactions between species, IL aggregates formation, and IL solubility using many more molecules than in DFT, given that quantum mechanics are much more computationally expensive to solve than Newtonian mechanics

2. OBJECTIVES

General objective:

- To find the underlying mechanisms by which ions influence the catalytic activity of halide-based ionic liquid catalysts in the formation of hexylene cyclic carbonate from CO_2 cycloaddition to hexylene epoxide, using molecular dynamics.

Specific objectives:

- To evaluate existing propylene epoxide and carbonate force fields in the literature.

- To construct hexylene epoxide and carbonate force fields for GROMACS package simulation using propylene epoxide and carbonate force fields as the starting point.

-To test ionic liquids solubilities by molecular dynamics in hexylene epoxide and carbonate, comparing results with the experimental evidence.

-To study interaction energies and radial distribution functions between key atom pairs in molecular dynamics simulations of different ionic liquids and hexylene epoxide.

3. MATERIALS AND METHODS

3.1 Force Fields

This section will present the force fields used for the different molecule species of this work. The molecular structures, short name labels, and CAS numbers corresponding to the organic species used in this work can be seen in **Fig. 8**. Ionic Liquid structures will be presented in the following sections.

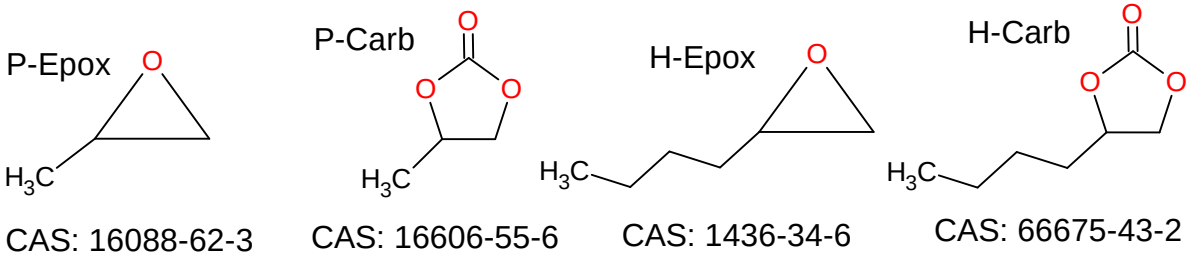

Figure 8. Molecular structures and generic CAS number identifiers for the organic species employed in the simulations of this work. P-Epox force field obtained from: https://atb.uq.edu.au/molecule.py?molid=37250#panel-md P-Carb force field obtained from: https://atb.uq.edu.au/molecule.py?molid=715057

No coarse-grained or united-atoms models have been employed. Therefore, all simulations correspond to atomistic simulations in which all-atom force fields have been employed.

3.1.1 Propylene Epoxide and Carbonate Force Fields

Propylene epoxide (P-Epox) and carbonate (P-Carb) force fields were found on the Automatic Topology Builder (ATB) public website **[51, 52]** (check **Fig.8** for details) ready for GROMACS simulation package. The topology files corresponding to both molecules contained non-standard atom types which are not included in GROMOS force field. Therefore, auxiliary files had to be loaded for simulation with an "include" statement. Nevertheless, and because this work aims to simulate mixed systems, Lennard-Jones parameters (σ and ε) were computed from the available $C_i^{(6)}$ and $C_i^{(12)}$ using the expressions:

$$\left.\begin{aligned} C_i^{(6)} &= 4 \cdot \epsilon_i \cdot \sigma_i^6 \\ C_i^{(12)} &= 4 \cdot \epsilon_i \cdot \sigma_i^{12} \end{aligned}\right\} \rightarrow \frac{C_i^{(12)}}{C_i^{(6)}} = \frac{\sigma_i^{12}}{\sigma_i^6}$$

Which result in the equations:

$$\sigma_i = \left(\frac{C_i^{(12)}}{C_i^{(6)}}\right)^{1/6} \qquad \epsilon_i = \frac{C_i^{(6)}}{4 \cdot \sigma_i^6} \qquad [\mathbf{Eqs.\,1, 2}]$$

These parameters were then introduced in the "[atomtypes]" and "[pairs]" sections. The combination rule was subsequently modified from 1 (Lennard-Jones potential described by $C_i^{(6)}$and $C_i^{(12)}$) to 2 (Lennard-Jones potential described by ϵ_i and σ_i), to achieve consistency for the use of Lennard-Jones interactions. By doing this, atom parameters are specified directly in the topology files, which will permit the construction of H-Epox and H-Carb force fields as will be explained in the next section.

3.1.2 Hexylene Epoxide and Carbonate Force Fields

Hexylene Epoxide (H-Epox) and Carbonate (H-Carb) are the compounds present in the experimental results **[29]** that will be used as references in this work. Therefore, their respective force fields were constructed by the combination of two force fields. For H-Epox the combination consists of P-Epox and the butylcyclopropane. H-Carb was correspondingly constructed by the combination of P-Carb and butylcyclopentane. This process has been schematized in **Fig. 9**.

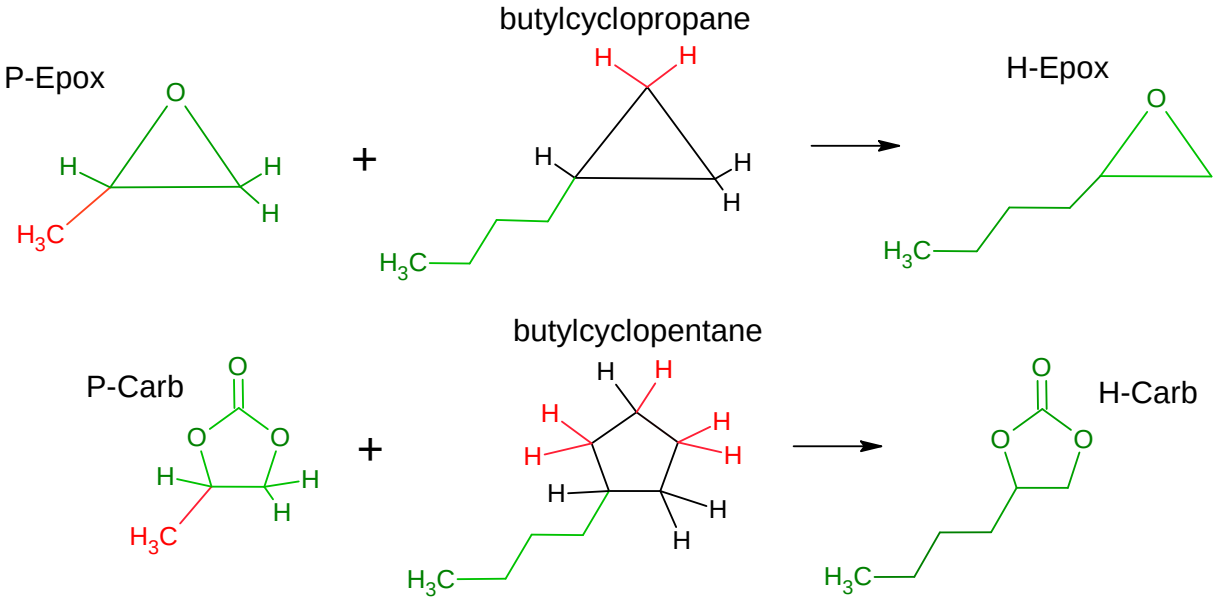

Figure 9. Schematic process of H-Epox and H-Carb force fields construction. In green, atoms taken from each structure along with the intramolecular interaction parameters between each other. In red, deleted atoms from the original structures whose intramolecular interactions were deleted from topology files. In black, atoms whose intramolecular interactions parameters were used for the final model construction.

Butylcyclopropane and butylcyclopentane force fields were also gathered from the ATB website **[51, 52]**. Lennard-Jones parameters were again calculated as specified in the previous sections. Once the parameters were determined, the combination was performed following several steps, the process will be exemplified for H-Epox, but the same methodology was used for H-Carb.

1. From the P-Epox topology file, all interaction lines relative to the atoms of the methyl side chain were deleted.

2. From the butylcyclopropane topology file, atoms belonging to the butyl chain were identified and added to the modified P-Epox topology file, renumbering them according to the previously remaining P-Epox atoms.

3. From the butylcyclopropane topology file, all interactions between atoms in the chain and between atoms of the chain with those in the cycle were taken and added to the modified P-Epox topology file with the corresponding new atom numbering. Interactions between atoms in the chain and non-existing atoms in the epoxide that could exist in the ring (i.e. hydrogens of CH_2 that disappear by the Oxygen of the epoxide in the position of that carbon) are excluded. Here an approximation is being made as the butylcyclopropane is

only composed of CH_2 groups. Intramolecular parameters describing flexion and torsion would slightly change for heteroatoms.

4. The geometry of the H-Epox molecule described in the .gro file is obtained by DFT geometry optimization. Atom numbering of this file is the finally employed, reason why the modified P-Epox topology file was again renumbered. The result of this last step is the H-Epox topology file.

5. Charges of each atom in the H-Epox topology file are set to those calculated by NBO over the DFT-optimized geometry. NBO was selected because of its similarity to the original charges present in the P-Epox file. Nevertheless, there are alternatives for charge calculation like Loewdin or Muliken. This step is essential to ensure the molecule has a zero net charge. This was not true for the constructed geometry of atoms belonging to different origin molecules. Charged groups interact through the Coulomb potential.

By following previous steps for the carbonate, the H-Carb force field was obtained.

3.1.3 Ionic Liquids Force Fields

Ionic Liquid force fields were obtained from a generic and systematic model available to be used interactively in the literature. More precisely, all cations and [Br] and [Cl] anions force fields were obtained through the Canongia Lopes & Padua (CL&P) model **[53, 54]**, which is based on the OPLS-AA/AMBER framework. This force field was constructed by the authors to achieve several specifications. These are:

Internal Consistency: All ions are parametrized with the same functional form. The equations underlying the model include the following potential energy expressions. For bonded interactions, stretch (bonded pairs) and bend (three consecutive atoms) are determined in the form of harmonic potentials:

$$U_{stretch} + U_{bend} = \sum_{ij}^{bonds} \frac{k_{r,ij}}{2} \cdot \left(r_{ij} - r_{0,ij}\right)^2 + \sum_{ijk}^{angles} \frac{k_{\theta,ijk}}{2} \cdot \left(\theta_{ijk} - \theta_{0,ijk}\right)^2 \qquad [\mathbf{Eq.\,3}]$$

While torsion is determined by dihedral angles between four consecutively bonded atoms, following the expression:

$$U_{torsion} = \sum_{ijkl}^{dihedrals} \sum_{m=1}^{4} \frac{V_{m,ijkl}}{2} \cdot \left[1 + (-1)^m \cdot \cos\left(m \cdot \varphi_{ijkl}\right)\right] \qquad [\mathbf{Eq.\,4}]$$

Non-bonded interactions are calculated as the contribution sum of Lennard-Jones and Coulombic interactions. The equation corresponds to:

$$U_{non-bonded} = \sum_{i}^{atoms} \sum_{j \neq i}^{atoms} \left\{ 4 \cdot \varepsilon_{ij} \cdot \left[\left(\frac{\sigma_{ij}}{r_{ij}}\right)^{12} - \left(\frac{\sigma_{ij}}{r_{ij}}\right)^{6} \right] + \frac{1}{4 \cdot \pi \cdot \epsilon_0} \cdot \frac{q_i \cdot q_j}{r_{ij}} \right\} \qquad [\mathbf{Eq.\,5}]$$

Equations in which r_{ij} and $r_{0,ij}$ correspond to distance and equilibrium distance respectively and $k_{r,ij}$ is the bond harmonic force constant. θ_{ijk} and $\theta_{0,ijk}$ correspond

to angle and equilibrium angle respectively and $k_{\theta,ijk}$ corresponds to angle harmonic force constant. φ_{ijkl} is the dihedral angle and $V_{m,ijkl}$ is the corresponding Fourier constant. σ_{ij} and ε_{ij} represent 12-6 Lennard-Jones parameters, ϵ_0 is the vacuum permittivity, and finally, q_i and q_j correspond to the atomic point charges. Within the same molecule, non-bonded interactions are exclusively considered for atoms separated by more than two bonds, being those separated by three scaled by a 0.5 factor. LJ interactions between different atom types are calculated by means of standard combination rules.

Transferability: Parameters are valid within ions of the same Ionic Liquid family and allow the possibility of ion interchange for different Ionic Liquids conception.

Compatibility: Molecular residue parameters are taken from established force fields, which enable the joining of neutral molecule parts into an existing ion.

For all these reasons CL&P was selected to be the model employed for the Ionic Liquids of this work. The future continuity of this work may address the use of CL&Pol model which corresponds to polarizable force fields, ready to use in LAMMPS software package. [I] anion was not included in the CL&P force field. Therefore, LJ parameters corresponding to this anion were extracted from OPLS-AA force field. Additionally, it was found that [Br] and [Cl] parameters used by default in the CL&P model corresponded exactly to those in OPLS-AA, reason why the [I] addition is justified.

3.2 Vapor-Liquid Densities Coexistence Method

The direct coexistence technique consists of an arbitrary number of simulations performed at different temperatures in the canonical ensemble (NVT). In each simulation, a vapor phase and a liquid phase are expected to be present, which will allow to determine both vapor and liquid densities coexisting in equilibrium. This result can then be compared with any source of reliable data to determine whether the force fields are correctly parametrized.

3.2.1 Propylene Epoxide Densities Coexistence Method

The initial configuration was generated by random molecule insertion into the simulation box using PACKMOL software package. Box dimensions and the number of molecules (N) were selected in terms of the cutoff radius (r_c) of 1.791 nm, which corresponds to a 5σ relation with the maximum σ in the simulation. The length of the simulation box along the *x*- and *y-axis* (L_x and L_y) were calculated from the selected r_c making sure minimum image convention (MIC) was satisfied for periodic boundary conditions (PBC) utilization, which corresponds to the use of the following relation:

$$L_x = L_y = 2.001 \cdot r_c \rightarrow L_x = 3.60\ nm \qquad \textbf{[Eq. 4]}$$

The final value used in the simulation was expanded to 3.80 nm to get more bulk. Once L_x and L_y have been determined, by using an experimental density (ρ) value of $820\ kg/m^3$, N can be set as a function of L_z by means of the following equation.

$$N = \frac{{L_x}^2 \cdot \rho \cdot N_A}{Mm} \cdot L_z = 122.8 \cdot L_z \qquad \textbf{[Eq. 5]}$$

Where Mm and N_A corresponds to the carbonate molar mass and the Avogadro's number respectively. L_z was chosen equal to 30σ to obtain a wide enough liquid slab so that the two vapor-liquid interfaces generated can be considered independent from each other. This corresponds to a length along the *z-axis* (L_z) of 10.8 nm. Finally, N was calculated using the previous relation obtaining a value of 1325 molecules.

The initial configuration randomly generated using the previous box dimensions and the number of molecules was minimized and used as the starting point in a simulation performed in the canonical ensemble (NVT) at 65ºC using the velocity-rescaling (v-rescale) thermostat. The next step was a simulation performed in the isothermal-isobaric ensemble (NPT), conserving the previous temperature. The pressure was controlled by a semi-isotropic Parrinello-Rahman (20 bar) barostat with a compressibility factor of 10^{-10} along the *x-* and *y-axis* axes while permitting fluctuation along the *z-axis* with a $4.5 \cdot 10^{-5}$ value. Once potential energy was stable, a last minimization was performed. Finally, an expansion in L_z was performed, generating empty space. The final box dimensions were 3.8 nm for L_x and L_y, while after the expansion L_z was 30 nm long.

The NVT coexistence technique simulations were carried out using v-rescale thermostat and a timestep of 0.002 ns during 10 ns of simulation time. Selected temperatures range from 200 K to 450 K with an increment of 50 K, which were used in corresponding NVT simulations. Long-range dispersion corrections were not applied in the simulations because there is more than one phase in the system.

3.2.2 Propylene Carbonate Densities Coexistence Method

The methodology employed in the previous section was reused for the carbonate. The initial configuration was generated with PACKMOL software package. Box dimensions and N were selected in terms of r_c, using the value that was used for simulating the epoxide (1.791 nm). This corresponds to a 5σ relation. L_x and L_y was selected allowing PBC utilization.

$$L_x = L_y = 2.001 \cdot r_c \rightarrow L_x = 3.60\ nm \qquad \textbf{[Eq. 6]}$$

The corresponding relation between N and L_z was determined, by using an experimental density (ρ) value of $1000\ kg/m^3$.

$$N = \frac{{L_x}^2 \cdot \rho \cdot N_A}{Mm} \cdot L_z = 76.45 \cdot L_z \qquad \textbf{[Eq. 7]}$$

L_z was maintained in 30σ, which corresponds to 10.7 nm. Finally, N was calculated, obtaining 825 molecules. To the randomly generated configurations, the same steps explained in the previous section were applied, resulting in the corresponding initial configuration for the NVT simulations. Selected temperatures range from 300 K to 700 K with an increment of 100 K between each. The final box dimensions were to 3.6 nm for L_x and L_y, while after the expansion L_z was set equal to 36 nm.

3.2.3 Propylene Epoxide Densities Coexistence Method

The methodology employed in this case was different, as no experimental value of density was known. The number of molecules (N) was selected arbitrarily to be 520, being these molecules inserted aleatory in a box that could contain them by using

PACKMOL software package. The obtained configuration was then minimized. The resulting minimized configuration was used in an NVT simulation with the same specifications as those explained in the previous sections. Then, the resulting configuration was replicated along the *z-axis* to ensure there were enough molecules to form a liquid phase, whose lateral interphases could be considered independent from each other. Therefore, the total number of molecules had been incremented to 1040 by this point. The resulting configuration was used in an NPT simulation with the same specifications as those employed in the previous section. Finally, the length of the simulation box along the z-axis, L_z, was expanded. The final box dimensions corresponded to 4 nm for L_x and L_y, while after the expansion L_z was set equal to 40 nm. All specifications employed in the NVT simulations using the direct coexistence technique are equivalent to those of the previous sections. Temperatures selected in this case range from 200 to 600 K with a temperature increment of 100 K.

3.3 Semi-isotropic NPT Simulations

Semi-isotropic NPT simulations were constructed for the solubility analysis of ionic liquids in both the epoxide and the carbonate together. Each simulation contains an ionic liquid composed of an anion and a cation combination in addition to the hexylen epoxide (H-Epox), and carbonate (H-Carb). A total of six simulations were carried out, which correspond to two cations ([N4444] and [N2222]) each one combined independently with the three halide anions ([I], [Br], and [Cl]). The initial configuration was constructed by the combination of three pre-simulated and stabilized systems, one for the Ionic Liquid, another for the epoxide, and another for the carbonate. The pre-simulation process consisted of several steps, applied to each of the pure phases. The process for each pure phase started with a minimization of the randomly generated configuration. The next step was a semi-isotropic NPT simulation in which a packed liquid configuration was obtained. Lastly, another minimization was carried out. Then, the three pure configurations were unified in a single simulation box, obtaining a configuration which was again minimized before simulation. This process was repeated two times, one for each cation. Once the configuration had been generated for each of the cations and [I] anion, the topology file parameters for [I] were changed to those of [Cl] and [Br], therefore facilitating the process. To achieve this, a combined topology file had to be created, including all parameters and atoms of the Ionic Liquids and those of H-Carb and H-Epox. Lennard-Jones parameters were employed for all the species, which is the reason why combination rule 2 was maintained, with pair generation. Lastly, fudgeLJ and fudgeQQ from the topology file were set to 0.5 which was the default value for the Ionic Liquids. The simulation details employed for “production” (even though it will be seen in the Results section that much more simulation time would be needed) correspond to a time step of 0.001 ns (lower than the one used in the previous section to better represent long alkyl chains flexibility), with simulation times around 50-100 ns (depending on the cation). The cutoff radius was selected to be equal to 1.35 nm, using long-range corrections. Coulomb interactions evaluation was performed by a fast smooth particle-mesh Ewald method (PME) which was set by default in the CL&P model. V-rescale thermostat and Parrinello-Rhaman barostat were selected at the experimental reaction conditions (65ºC and 20 bar). The number of molecules of each component corresponds to 500 H-Epox and 250 H-Carb for the organic species. For [N4444] cation 200 cations and

therefore 200 anions were employed, while for [N2222] 250 cations and anions were employed because of the reduced longitude of the side chains of this cation.

3.4 Isotropic NPT Simulations

Isotropic NPT simulations were performed aiming to analyse the interaction energies and radial distribution functions (RDFs) between several atom pairs that were considered crucial for the reaction process in the literature. For these simulations, ionic liquids and H-Epox were the only species used, excluding H-Carb from the analysis. Simulation boxes were constructed by the random insertion of ionic liquid molecules (200 cations and 200 anions) in an oversized simulation box. Then, H-Epox molecules were randomly inserted (600 H-Epox molecules) in the configuration containing the Ionic Liquid. Lastly, the resulting configuration was minimized. This procedure was followed to obtain a mixed configuration in which diffusion would have already occurred, skipping the mixing step that in the previous section was found to be very slow. The simulation details utilized in these simulations are those specified in the previous section. A total of nine simulations were performed, three for each cation corresponding to each halide anion. Three cations were studied: [N4444], [emim], and [bmim], whose structures will be shown in subsequent sections of this work.

4. RESULTS AND DISCUSSION

4.1 Epoxides and Carbonates Force Fields

4.1.1 Liquid-Vapor phase equilibrium of Propylene Epoxide and Carbonate

Propylene Epoxide (P-Epox) and Carbonate (P-Carb) force fields taken from the ATB public website have been evaluated in terms of their pure Vapor-Liquid equilibrium properties by the density's coexistence method. Results for both evaluations will be presented and discussed in this section. The visual inspection of the P-Epox NVT simulation boxes with temperatures 200 and 400 K can be observed in **Fig. 10**. The visual inspection for 200 and 700 K of the homologous simulations for the P-Carb force field is shown in **Fig. 11**.

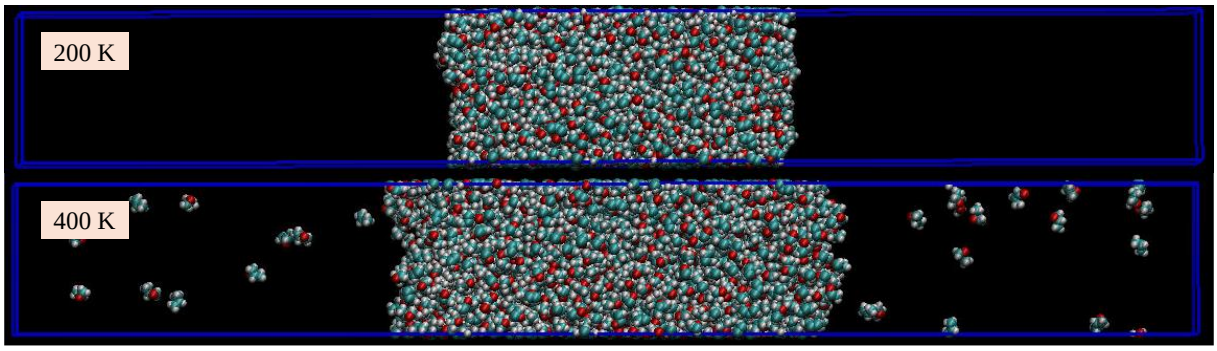

Figure 10. Visual inspection of P-Epox NVT simulation boxes at 200 and 400 K.

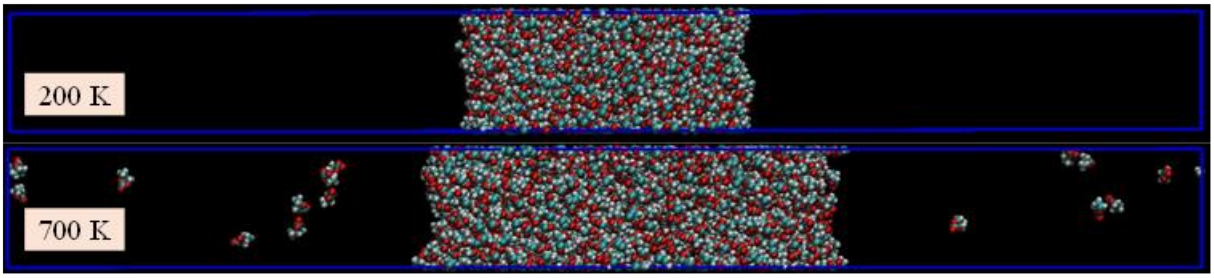

Figure 11. Visual inspection of P-Carb NVT simulation boxes at 200 and 700 K.

By observing **Fig. 10** and **Fig. 11** it can be noted that at 200 K there is no vapor phase in coexistence with the liquid neither for P-Epox or P-carb. Therefore, the liquid phase remains packed in the center of the box with negligible vapor pressure. On the other hand, at 400 K for P-Epox and 700 K for P-Carb a vapor phase is visible in the form of moving molecules through the whole z axis. Additionally, liquid phases occupy a greater extension. This means liquid phases are composed of fewer molecules that occupy a greater volume, which is why a reduced density is expected to be found in the liquid phases at these temperatures for both systems. By comparing P-Epox at 400 K and P-Carb at 700 K, it is notable that fewer molecules can move from the liquid to the vapor phase in the latter, even though the temperature difference of 300 K. This implies P-Carb will be less volatile than P-Epox. The density profiles resulting from the different temperatures are shown in **Fig. 12** for P-Epox and in **Fig. 13** for P-Carb.

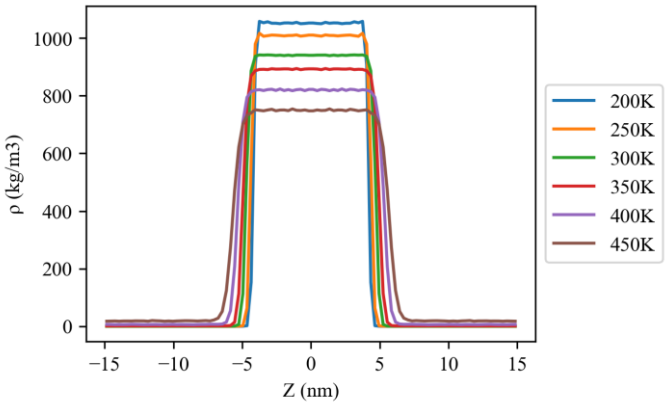

Figure 12. Density profile results for P-Epox force field Vapor-Liquid equilibrium validation.

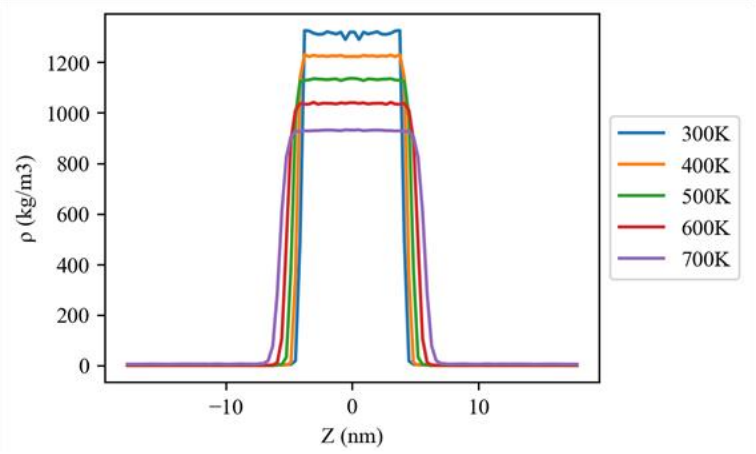

Figure 13. Density profile results for P-Carb force field Vapor-Liquid equilibrium validation

The density profiles obtained in **Fig. 12** and **Fig. 13** correspond to what was expected to be found. For greater temperatures liquid densities (top stable values of the curves) find a lower value, while gas densities (curve bases) increase by displacing in the vertical axis. Additionally, interphase (transition zones between curves bases and tops) thicknesses get bigger. This trend is conserved from 200 to 450 K for P-Epox temperatures. From each curve in in **Fig. 12** and **Fig. 13** a liquid and a vapor density can be obtained through the average of the values encountered at the top and the bottom separately. Obtained equilibrium V-L densities can then be plotted against experimental data or any alternative model. For this work, experimental values found for the liquid phases were gathered, which were validated by the Peng-Robinson Equation of State (EoS) for the liquid, being this model used afterward for the gas density prediction. Densities obtained by Molecular Dynamics (MD) compared to both experimental and Peng-Robinson (PR) predictions can be seen in **Fig. 14a** for P-Epox and in **Fig. 15a** for P-Carb. P-T diagrams can also be generated by attending to the transversal pressure of the simulation boxes along the z-axis for each temperature. Experimental and Peng-Robinson values compared with MD results can be found in **Fig. 14b** for P-Epox and in **Fig. 15b** for P-Carb.

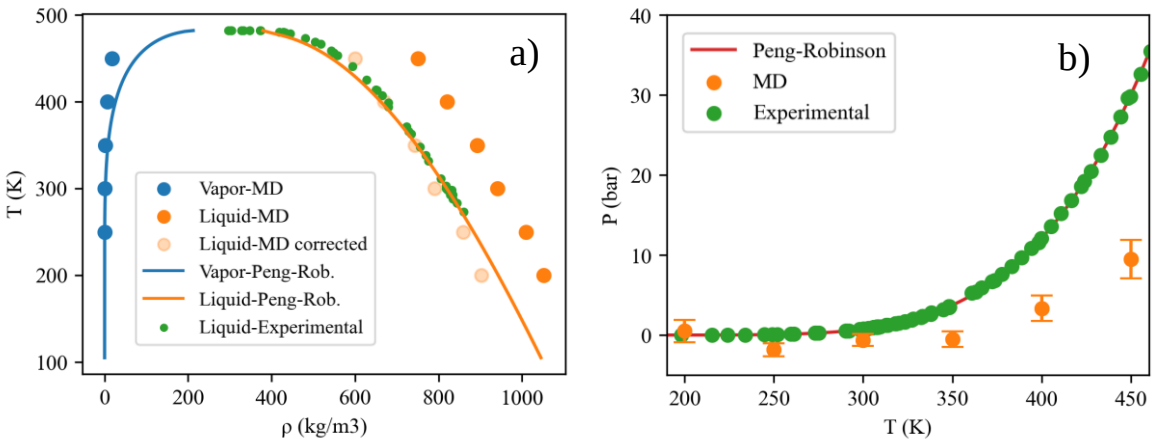

Figure 14. a) P-Epox MD densities obtained from the density profiles compared to experimental **[55]** and PR. EoS prediction **[59]**. Corrected values are obtained from 150 Kg/m^3 subtraction to the obtained Liquid-MD values. b) P-Epox MD P-T phase diagram result compared with experimental data **[56]** and PR predictions **[59]**.

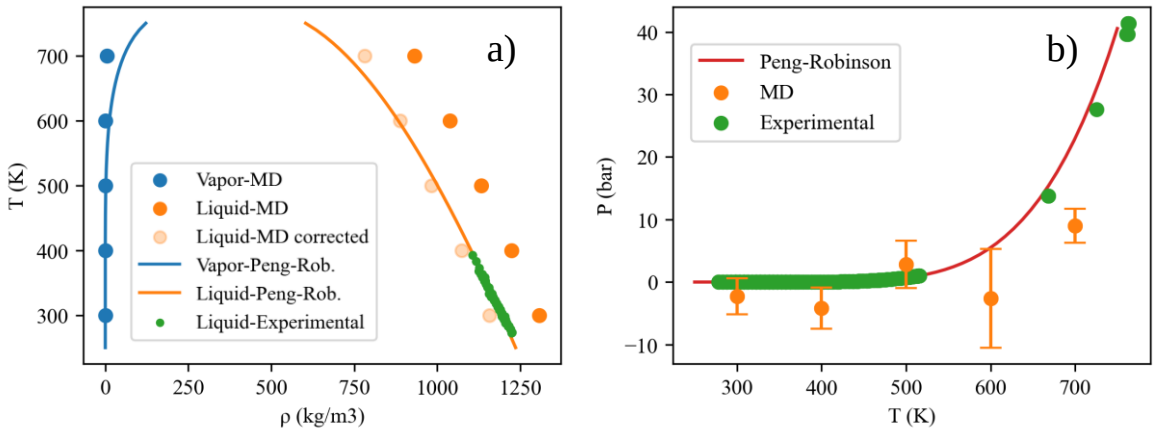

Figure 15. a) P-Carb MD densities obtained from the density profiles compared to experimental **[57]** and PR EoS prediction **[59]**. Corrected values are obtained from 150 Kg/m^3 subtraction to the obtained Liquid-MD values. b) P-Carb MD P-T phase diagram result compared with experimental data **[58]** and PR predictions **[59]**.

Attending to **Fig. 14a** and **Fig. 15a,** experimental data is in great agreement with Peng-Robinson predictions for the liquid phase, therefore some confidence may be gained about predicted gas densities. By comparing MD densities with those predicted by Peng-Robinson, vapor densities are slightly underestimated, especially for 400 and 450 K for P-Epox and for 700 K for P-Carb. Correspondingly, liquid densities are overestimated for both compounds by 150 Kg/m^3 as demonstrated by the corrected MD points generated by the subtraction of that quantity from the obtained MD densities values. The force field models are then capable of reproducing the densities trend visible in the phase diagram, even though densities are displaced from the expected, reason why model refinement and reparameterization are convenient. Additionally, the MD densities curve shapes in both P-Epox and P-Carb seem to be overestimating the critical points. In terms of the P-T phase diagrams visible in **Fig. 14b** and **Fig. 15b**, once again Peng-Robinson perfectly describes the P-T curves, while MD poorly follows an approximate trend for P-Epox with a slight improvement for P-Carb, being pressures underestimated in both cases. Negative pressures have been obtained for the lowest temperatures, which shows the difficulty of pressure determination for very low partial pressures by GROMACS software package, which would probably be corrected by longer simulation times, obtaining far more data for the pressure averaging. P-T diagrams results show again the need for reparameterization, and force field improvement given that expected experimental values are not exactly reproduced. Improvements performed over one of the force fields may be applicable to the other, as deviations are similar, and most of the atoms are shared between both compounds. Nevertheless, and because the results are qualitatively correct, both force fields will be used in the subsequent sections of this work.

4.1.2 Hexylene Epoxide (H-Epox) Force Field

The Hexylene Epoxide (H-Epox) force field was constructed as the combination of P-Epox and butyl-cyclopropane force fields along with atom charges substitution to those obtained by NBO calculation after DFT geometry optimization, ensuring that the molecule has net charge zero. The resulting force field is evaluated in this section by the density's coexistence method following the methodology employed previously for P-Epox and P-Carb. The visual inspections for the NVT simulations performed at 200 and 500 K for H-Epox correspond to **Fig. 16**. This figure constitutes a satisfactory result given that for the greater temperature a vapor phase is formed. The corresponding density profiles obtained for the different temperatures can be seen in **Fig. 17**. Density profiles were used to obtain the V-L coexistence densities applying the same averaging criteria employed for P-Epox and P-Carb. Resulting densities along with the P-T phase diagram can be seen in **Fig. 18a** and **Fig. 18b** respectively, compared only with Peng-Robinson predictions as no experimental data were found.

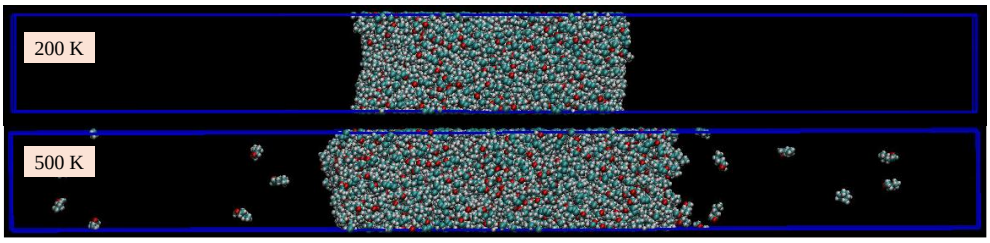

Figure 16. Visual inspection of H-Carb NVT simulation boxes at 200 and 500 K.

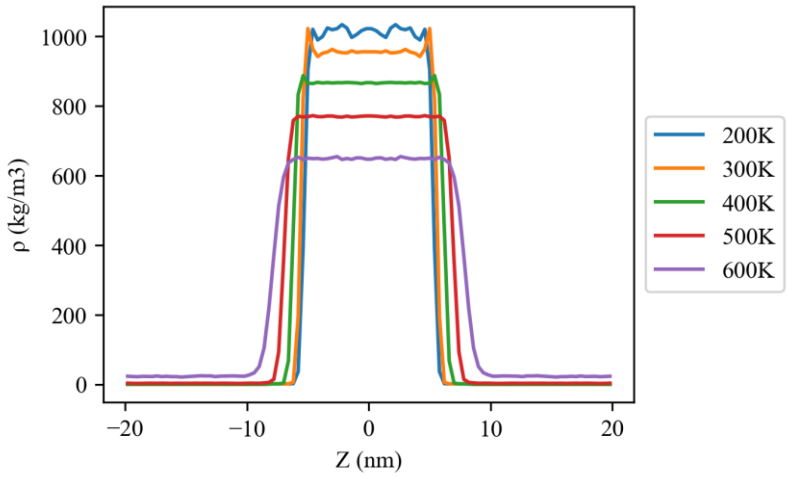

Figure 17. Density profiles result for H-Epox constructed force field.

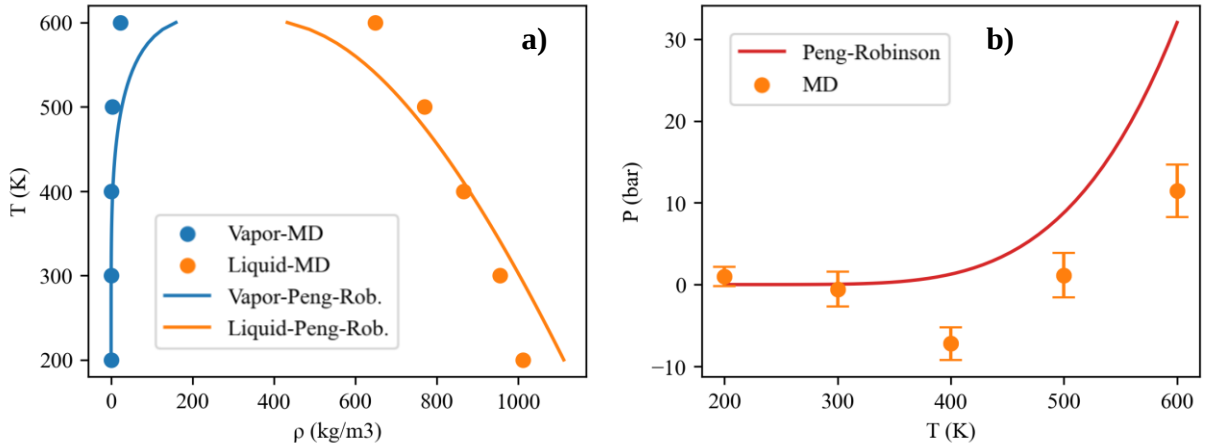

Figure 18. a) H-Epox MD densities obtained from the density profiles compared to PR EoS predictions **[59]**. b) H-Epox MD P-T phase diagram result compared with PR predictions **[59]**.

The results visible in **Fig.18a** show the great impact of the changes performed to P-Epox to obtain the H-Epox force field. If Peng-Robinson's predictions are correct, gas densities remain underestimated for the greater temperatures (500 and 600 K), while liquid densities are underestimated for 200 and 300 K and overestimated for 500 and 600 K, being the density value at 400 K almost equal to that of Peng-Robinson prediction. Additionally, the critical point is overestimated given that PR situates it in the vicinity of 600 K. These results contrast with those obtained for the P-Epox force field, in which liquid density values were displaced by 150 kg/m^3. H-Epox densities seem to be numerically closer to PR predictions in this case. The interval comprehended between 300 and 500 K is the one that better reproduces densities, and luckily, experimental conditions (65 ºC) that will be tried to be reproduced in the following sections containing the ionic liquid, H-Epox and H-Carb molecules are situated in this temperature range, which may justify the utilization of the constructed force fields. **Fig. 18b** shows like in the previous homologous diagrams that P-T behaviour is poorly reproduced with a lot of uncertainty for reduced pressures. Much more simulation time should be employed to obtain more certain pressure results. It should be noted that force field refinement could be and in fact, should be performed over the obtained model. For example, charge reparameterization was made by selecting NBO-calculated charges merely because their values were the most similar

to the atomic charges originally present in the P-Epox force field. But there are other available methods which find quite different charge values, that will surely change resulting properties, maybe improving results. Nevertheless, it should be kept in mind that MD values are being compared with PR predictions which have not been validated by experimental results. Therefore, a lot of uncertainty is present in the analysed results, even though, at least qualitatively, the model seems correct.

4.2 Solubility Analysis

Ionic liquids solubilities in hexylene epoxide (H-Epox) and hexylene carbonate (H-Carb) were studied for [N2222] and [N4444] cations combined independently with the three halide anions [I], [Br] and [Cl]. This constitutes a total of six semi-isotropic NPT simulations at the experimental conditions (65ºC and 20 bar) with three initial independent phases of H-Epox, IL, and H-Carb distributed along the z-axis. For better visualization of the ionic liquid molecules, H-Epox and H-Carb have been excluded from the visual inspections of the simulations. Nevertheless, they are present as shown in **Fig.19**, being H-Epox represented in pink and H-Carb in white colours. H-Epox results miscible in H-Carb as was expected to happen.

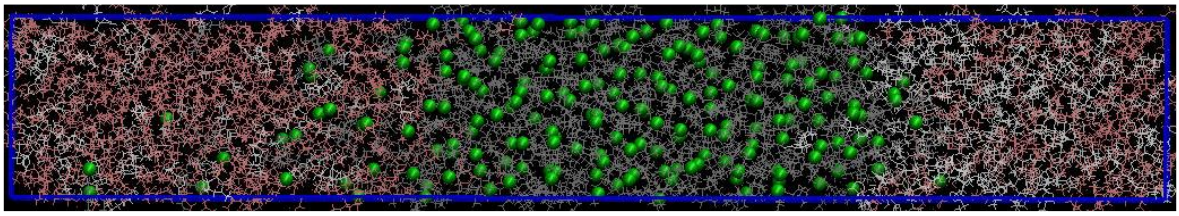

Figure 19. Visual Inspection of [N4444][Br], H-Epox (pink) and H-Carb (white) semi-isotropic NPT simulation. H-Epox and H-Carb models result mutually soluble from the initial independent pure phases.

4.2.1 Solubility Analysis of [N2222] [I/Br/Cl]

The visual inspection of the final configurations of [N2222] cation combined with [I], [Br], and [Cl] anions, excluding H-Epox and H-Carb from the representation can be seen in **Fig. 20**.

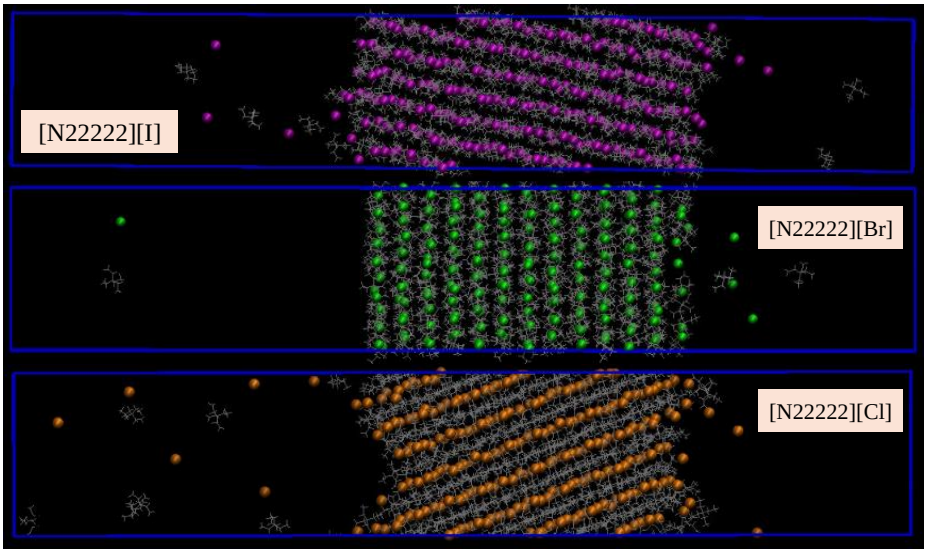

Figure 20. Visual inspection of semi-isotropic NPT simulations of [N2222] [I/Br/Cl], H-Epox and H-Carb. Last two are excluded from the representation for improved Ionic Liquid visualization.

Fig. 20 shows that the three ionic liquid systems have crystallized. Cations and anions are therefore distributed in regular structures, which implies a low or negligible solubility of these ionic liquids into the epoxide or the carbonate. This result constitutes the first validation of the molecular models employed in this work, as the three ionic liquids were experimentally determined to be insoluble, as presented in **Table 1** and **Fig. 6a**. Additionally, experimental results found very low carbonate yields for these Ionic Liquids (**Fig. 6a**), varying from 1% for [N2222][I] to 4% for [N2222][Cl]. Therefore, it becomes obvious that, for insoluble ionic liquids, epoxide conversions will be low. The catalyst is not able to properly interact with the epoxide for reaction, situation that was supported experimentally and theoretically confirmed by the results obtained in this work. Nevertheless, some additional comments should be made about these simulations. First, system dynamics were extremely slow, taking Ionic Liquids molecules diffused into the epoxide and the carbonate large times to change their positions in the simulation boxes. Secondly, it is remarkable that the crystallization event in [N2222][Cl] was by far the slowest among the halides, visible in **Fig. 21** as the drastic energy diminution before 20 ns, while for [I] it occurred at the beginning. This phenomenon can be merely attributed to difficulties in a solid nuclei formation for the subsequent propagation of the solid phase, but a greater number of cations and anions have achieved diffusion into the epoxide and carbonate (**Fig. 20**). This apparent greater solubility concerning the other halides is also present in the carbonate yield experimental data, being [N2222][Cl] slightly more reactive than the others. Nevertheless, this might just be a matter of time and after much more simulation time free cations and anions could end up joining to the solid phase. But as it has been said, the dynamics encountered were slow, reason why this result could not be confirmed. Finally, by observing **Fig. 20** it appears that even though anions mobility should be superior to cations as they are single-atom ions, it looks like the diffused number of cations and anions is somehow equivalent. This in fact may have greater implications than expected, as solubility might be dominated by the more voluminous cation's diffusion capability, while halide anions could follow diffused cations forming either ion pairs or aggregated species in some proportion, being the first case visible in **Fig. 20** representations. Observing again **Fig. 20**, it looks like cations somehow delimitate the space where halide anions diffuse, the cation-anion interaction may be playing a very significant role in solubility.

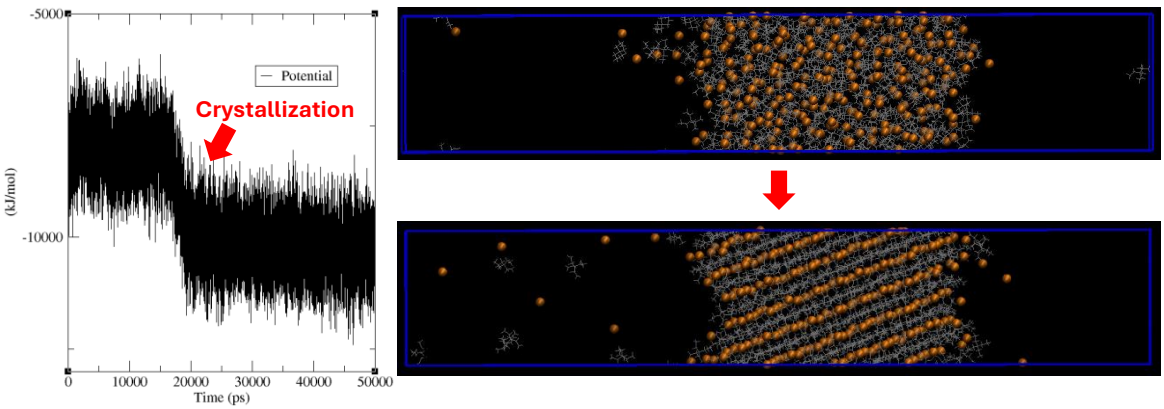

Figure 21. Potential Energy over simulation time and crystallization event for [N2222][Cl] Ionic Liquid simulation.

4.2.2 Solubility Analysis of [N4444] [I/Br/Cl]

The visual inspection of the final configurations for [N4444] cation combined with the three different halides can be observed in **Fig. 22**. H-Epox and H-Carb were again excluded from the representation to achieve improved visualization. Attending to **Fig. 22**, ionic liquid phases remain disordered after the simulations, even with visible diffusion of the Ionic Liquids in the H-Epox and H-Carb medium. Therefore, crystallization has not happened, meaning this ionic liquids are miscible in the H-Epox and H-Carb phase. This constitutes another validation of the employed force fields, as experimentally (**Table 1** and **Fig. 6a**) it was found that [N4444][Br] and [N4444][Cl] should be soluble in both the epoxide and the carbonate, while [N4444][I] was expected to be soluble after reaction, which is the case in these simulations, as a fraction of carbonate product is present in the boxes. Nevertheless, it should be noted that once again the system dynamics were very slow, needing ionic liquid cations and anions long simulation time to move through the organic phases. This is the reason why a homogeneous distribution of the ionic liquids is not still visible, much more simulation time is needed to find the real equilibrium state at which the energy truly stabilizes within a constant value. It is remarkably important how the diffused cation-anion distribution resembles the one introduced for [N2222] cation in the previous section. If halide anions were expected to have greater mobility than [N2222] cation, it should be even more notorious for [N4444] cation in which side alkyl chains have lengthened in two carbons each. But again, attending to **Fig. 22**, a homogeneous distribution of the halide anions is not found.

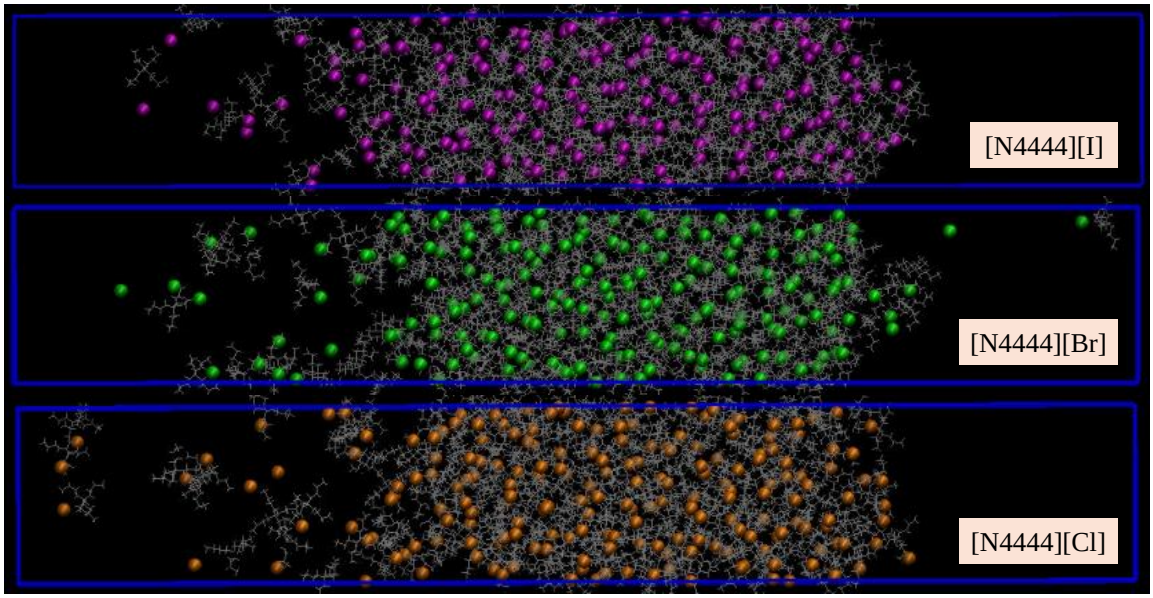

Figure 22. Visual inspection of semi-isotropic NPT simulations of [N4444] [I/Br/Cl], H-Epox and H-Carb. Last two are excluded from the representation for improved Ionic Liquid visualization.

It looks like cations diffusion is what widens the halide anion's mobility range, forming ionic pairs instead of dissociated species. This is in fact in great correspondence with the low conductivities found experimentally, or the also low dissociation constants computed with DFT/COSMO-RS. The results found for these simulations point in the direction that independent cations and anions should not be considered the only reactive species in these systems, as their presence is very reduced and does not

explain conversions of up to 90%. The ionic pairs may be the true catalyzers of this reaction, being these species much more common in the simulations performed in this work and supported by what are to date the most successful descriptors of the catalytic activity, which are experimental conductivities and the calculated ionic liquids dissociation constants. The results obtained in this section for [N4444] cation along with those found for [N2222] cation in the previous section show something relevant. Simulations performed with [N2222] cation eventually crystalized for the three halide anions, while those performed with [N4444] cation with the same halide anions did not. It can therefore be concluded that solubility is being determined by the cation, which is the only differentiating element, and to be more specific, it is the side chain lengths that is changing and therefore influencing the solubility. It looks like longer side chains improve ionic liquids solubility, at least in an H-Epox and H-Carb medium, which of course has an enormous impact on catalytic activity, being soluble Ionic Liquids expected to be far more reactive with epoxide than insoluble ones. This is in fact what was found experimentally (**Table 1** and **Fig. 6a**) with carbonate yields varying from 91% from [N4444] [I] to 1% for [N2222] [I] and confirmed now theoretically for both [N2222] and [N4444] cations combined with the three halide anions. Then it can be concluded that ionic liquids solubility and cation-anion interaction play a primary role in the catalytic activity and that it is mainly influenced by both cation and anion structures, being ionic pairs between cations and anions or ionic liquids aggregates the most common species in reaction media. It should be noted that the solubility mechanism has not yet been confirmed. Given that halide anions are common between simulations and that solubility has changed when cation was varied, it is possible that cation interaction with H-Epox and H-Carb is what changes solubility, being [N4444] chains more like the epoxide and carbonate alkyl side chain. But another possibility indeed is that the cation-anion interaction strength is changing solubility, given that if this interaction is too strong, the ionic liquid will try to remain in the form of aggregates rather than as free ion species or ionic pairs. Therefore, there is still a need to truly determine the real mechanism relying on the cation effect. Finally, it is important to remark that much more simulation time is needed, in the search of real equilibrium results rather than the stationary states that have been presented, even though many molecular insights have been gained by simply observing the simulation boxes and differences between cations.

4.3 Reaction Medium Interactions

In the previous section, satisfactory results for ionic liquid solubilities in comparison with experimental results have been obtained, this constituted the force field models validation, which enables further investigations. In this section, a better understanding of the catalytic activity displayed by halide anion variation and the cation effect will be searched. The motivation to achieve this is that knowledge of the underlying mechanisms that determine catalytic activity enable the molecular design towards its improvement. In this section, several Radial Distribution Functions (g(r)) will be computed in terms of different reference atoms or atom groups. **Fig. 23** specifies the selected atoms and the nomenclatures employed afterward.

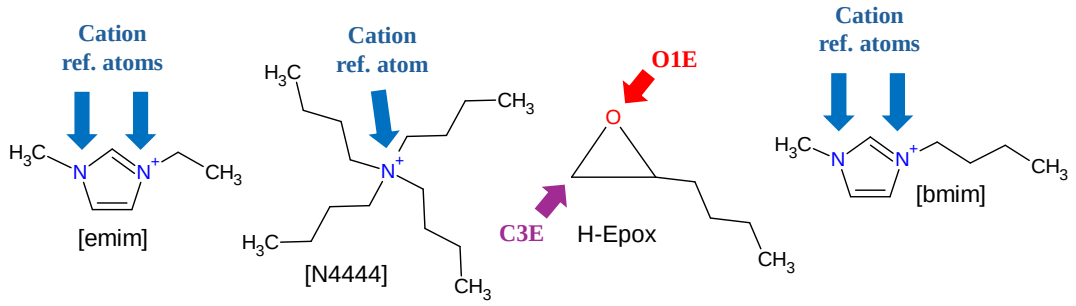

Figure 23. Structures, reference atoms, and nomenclature employed in Radial Distribution Functions (RDFs).

The halide anion effect will be investigated for three different cations independently. These cations will be the previously studied [N4444] cation and the newly incorporated [emim] and [bmim], both presented in the introduction of this work and with available experimental data. Atom pairs selection for radial distribution functions construction has been made based in what was previously hypothesized in literature that could be influential in the reaction mechanism (**Fig. 3** and **Fig. 4**). Therefore, selected pairs are:

1. Cation reference atom relative to the halide anions (**Cation ref. atom-halide**). Expecting to determine which halides interact more frequently with the cation reference atom, *i.e*, cation-anion interactions, which can be understood as more associated atoms.

2. Halide anion relative to the reactive carbon in the epoxide (**Halide-C3E**). Expecting to determine which halides are situated closer (anion-epoxide interaction) and with greater probability to the reactive carbon that will cause the epoxide ring opening for reaction in the first mechanism steps.

3. Cation reference atom relative to the epoxide oxygen (**Cation ref. atom-O1E**). Expecting to determine which cations are situated with more probability near the oxygen of the epoxide (cation-epoxide interaction), which is thought to cause epoxide activation before the nucleophilic attack of the halide anion.

The same methodology has been applied to the three cations combined with the halide anions. Results will be presented as two case studies based on cations similarity.

Case Study I: [N4444] [I/Br/Cl]

The radial distribution functions correspond to the three sets shown in **Fig. 24**. Mean interaction energies as the sum of the coulombic and Lennard-Jones interaction have been calculated between the cation Nitrogen (reference atom in the cation) and two other atoms in each simulation, the halide anion, and the epoxide oxygen. The resulting values along with the reported dissociation constant, ionization degree, and carbonate yield from the literature **[29]** are shown in **Table 2**. [N4444] based ionic liquids have been demonstrated to be soluble in the H-Epox and H-Carb medium in the previous section. Nevertheless, there is still a lack of an explanation about the influence of the different halide anions over catalytic activity which was demonstrated experimentally to follow the trend: [I]>[Br]>[Cl] (**Fig. 6**) (this is the case for all the ionic liquids studied in this section), while DFT calculations predicted energy barriers that would result in the opposite [I]<[Br]<[Cl] (**Fig. 5**), corresponding this last trend to the nucleophilic

character of the halide anions in an aprotic medium. Radial distribution functions were calculated to see how correlated positions are between selected atom pairs, trying to understand the microstructure of the system.

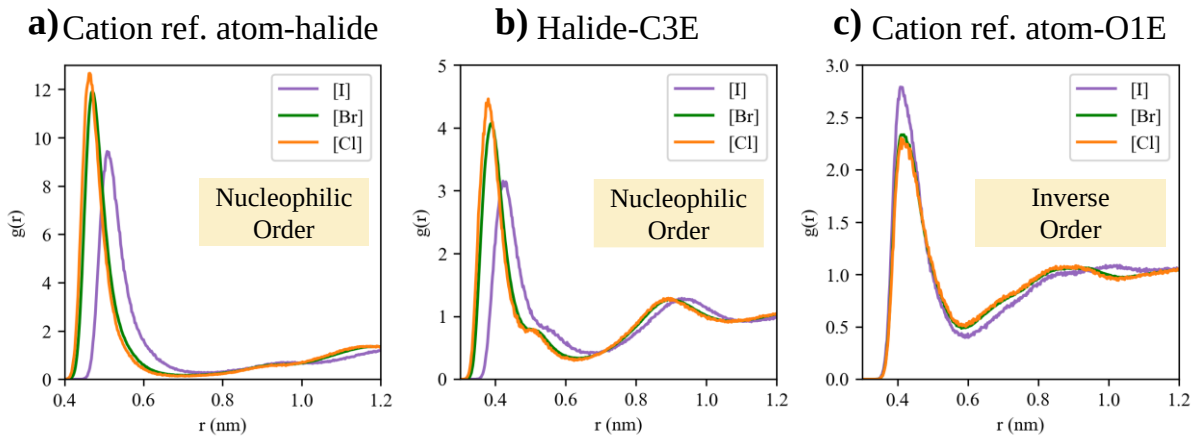

Figure 24. Radial distribution functions for [N4444][I/Br/Cl] simulations. Selected atom pairs: a) Cation reference atom-halide anion (cation-anion interaction) b) halide anion-reactive carbon in H-EPOX (anion-epoxide interaction) c) Cation reference atom-Epoxide Oxygen (cation-epoxide interaction).

Table 2. Carbonate Yield, Ionization degree (ξ), dissociation constant (KD), and Molecular Dynamics average interaction energies between selected atom pairs for [N4444] [I/Br/Cl] ionic liquids.

Ionic Liquid	Yield (%)[29]	ξ (%)[29]	KD [29]	$E_{cation-anion}$ (kJ/mol)	$E_{cation-O1E}$ (kJ/mol)
[N4444] [Cl]	29	0.80	$9.79 \cdot 10^{-7}$	-2024	-1178
[N4444] [Br]	76	1.09	$6.56 \cdot 10^{-5}$	-1875	-1177
[N4444] [I]	91	1.37	$4.41 \cdot 10^{-3}$	-1362	-1209

Calculated RDFs for each selected atom pair, for each of the three NPT isotropic simulations (one for each halide anion) can be seen in **Fig. 24**. It should be noted that the vertical axis scales in **Fig. 24** subplots are not equal. The scale difference between the RDFs of the Cation ref. atom-halide set compared with the other sets is more than doubled. Therefore, cation-anion interaction is by far the most probable interaction, meaning that in these ionic liquid systems, the anions are forming ionic pairs or aggregates. The narrow peaks of **Fig. 24a** reveal a predominant short cation-anion distance between ionic liquid species in reaction media, corresponding to the ion pairs observed previously in **Fig. 22**. As said before, this result is a validation of the employed force fields, as ionization degrees (calculated from experimental conductivities) and dissociation constants found very low values (**Table 2**). Additionally, for the Cation ref. atom-halide (**Fig. 24a**) and the Halide-C3E (**Fig. 24b**) RDFs sets, the first peaks are higher for [Br] and [Cl] than for [I], therefore having a greater area under the curve, which can be understood as the number of species that form the first coordination sphere around the reference atom. These results have two important implications.

Firstly, it means that [Br] and [Cl] anions are slightly more associated with the [N4444] cation (**Fig. 24a**). Secondly, it also means that [Br] and [Cl] are more probable to be found around the reactive carbon of the epoxide (**Fig. 24b**). The first result is promising to explain the experimental catalytic activity trend. This is because the most

experimentally reactive halide, which corresponds to [I], is also the one that is supposed to be less associated with the cation in the simulations, meaning more mobility and therefore better availability for reaction. This result constitutes another validation of the force fields, given that conductivity measurements and dissociation constants follow this trend too (**Table 2**). An alternative way to demonstrate that in the simulations [Br] and [Cl] anions interact stronger with the cation than [I] anion is by the interaction energy of the atom pairs (**Table 2**). It can be seen that cation-anion interaction energies are negative, which was expected given that both ions have opposite sign charges (attractive interaction energy), and are ordered in absolute value as the experimental catalytic activity trend: [I]<[Br]<[Cl]. This means that both RDFs and cation-anion interaction energies are in great correspondence and can explain the experimental catalytic activity. But surprisingly, as it has been said, RDFs of **Fig. 24b** find that [Br] and [Cl] are more likely to be found around the reactive carbon of the epoxide. So even though cation-anion interaction is telling [Br] and [Cl] are more attached to the cation and therefore should be less available for the reaction, it is additionally found that both are situated closer and with greater probability to the reactive carbon. Two possibilities arise from this situation. The first possibility is that even though these anions are more capable of performing the nucleophilic attack on the epoxide, the intermediate formation (**Int1**) in which the anion is covalently bonded to the epoxide is impeded because the cation is strongly interacting with the anion and therefore not letting it to move out in the search of a better life. The second possibility is the result obtained in the third set of RDFs in **Fig. 24c**. This result shows that in [N4444][I] simulation, the cation reference atom is situated with greater probability nearer the epoxide oxygen, maybe promoting the epoxide activation. This was a topic of discussion in the bibliography (**Fig. 4**) and has been surprisingly confirmed in this work, not only by RDFs but also by interactions energies between the cation and the epoxide as shown in **Table 2**, being the simulation with [I] halide the one that displays a slightly more attractive interaction between the cation and the Oxygen. This vision aligns with the reaction mechanism that proposes the epoxide activation as the first step, promoting afterward the nucleophilic attack of the anion. Both explanations seem rather plausible and in fact are not mutually exclusive. If cation-anion interaction is reduced and anions try to situate near the reactive carbon, the cation will be able to interact better with the oxygen because of its better mobility than in a situation in which it is nailed to the anion.

Case Study II: [emim] [I/Br/Cl] and [bmim] [I/Br/Cl]

RDFs for [emim][I/Br/Cl] and [bmim][I/Br/Cl] simulations correspond to the six sets shown in **Figs. 25** and **26**, respectively. The homologous table to the one presented for [N4444] cation in the previous case study corresponds to **Table 3** for [emim] [I/Br/Cl] and [bmim] [I/Br/Cl] ionic liquids. It is very important to highlight that for the energy calculation a single Nitrogen (**SN**) of the two selected as the reference atoms is considered. This selection was made before noticing both Nitrogens were representative in [emim] and [bmim] cations. To obtain the specific energy values for both atoms, simulations would have to be re-runed.

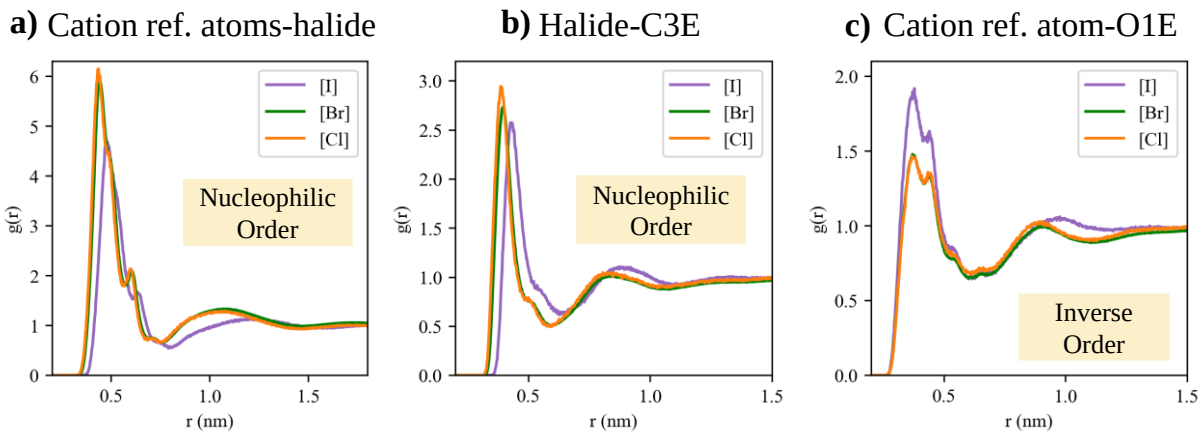

Figure 25. Radial distribution functions for [emim] [I/Br/Cl] simulations. Selected atom pairs: a) Cation reference atoms-halide anion b) halide anion-reactive carbon in H-Carb c) Cation reference atoms-Epoxide Oxygen.

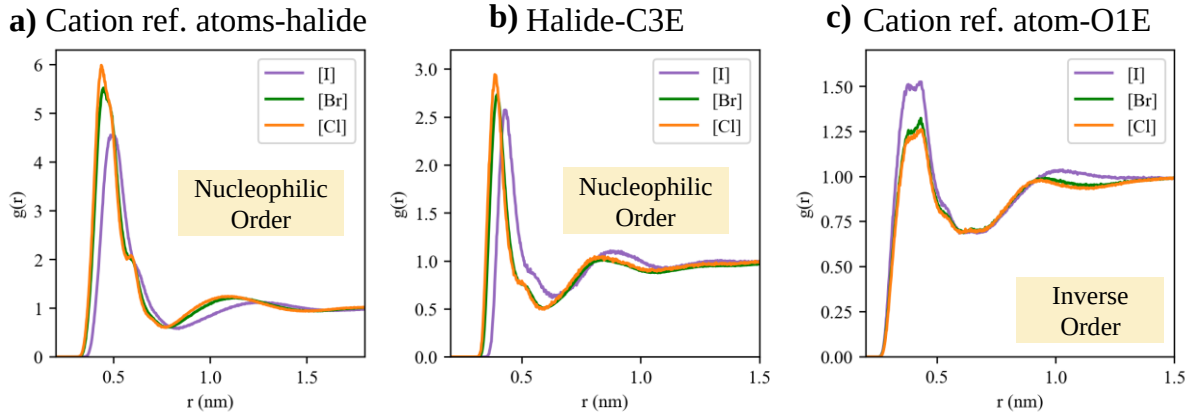

Figure 26. Radial distribution functions for [bmim] [I/Br/Cl] simulations. Selected atom pairs: a) Cation reference atoms-halide anion b) halide anion-reactive carbon in H-Carb c) Cation reference atoms-Epoxide Oxygen.

Again, the cation-anion interaction predominates and follows the order [I]<[Br]<[Cl] (**Table 3**). This means that imidazolium-halide-based ionic liquids also form ionic aggregates, probably ion-pairs attending to RDFs shapes in **Figs. 25a** and **26a**. MD results for [emim] and [bmim]-based ionic liquids are again in agreement with the very low ionization degrees, experimentally estimated by conductivity measurements and theoretically demonstrated by DFT/COSMO-RS by the calculation of ionic liquid dissociation constants (**Table 3**). Furthermore, the trend found in the cation-anion interaction energies ($E_{SN\text{-}anion}$ in **Tables 2** and **3**) is [emim]>[bmim]>[N4444] for each halide anion independently, explaining the lower solubility in reaction media and lower catalytic activity found in these imidazolium-based ionic liquids. Additionally, slightly stronger cation-epoxide interaction energies were found for [I] than for [Br] and [Cl] anions. This can be visualized in **Figs. 25c** and **26c** in the form of radial distribution functions, and in the interaction energies $E_{SN\text{-}O1E}$ in **Table 3**, which follow the catalytic activity trend of the epoxide conversion reaction. Therefore, MD results for imidazolium-based ionic liquids also indicate the main role of cation is the epoxide activation, therefore a stronger cation-anion interaction results in the reduction of the cation availability to stabilize the epoxide oxygen and the subsequent nucleophilic attack of the anion.

Table 3. Carbonate yield, ionization degree (ξ), dissociation constant (KD), and Molecular Dynamics average interaction energies between specific atom pairs for [emim] [I/Br/Cl] and [bmim] [I/Br/Cl] ionic liquids.

Cation	Anion	Yield (%)[29]	ξ (%)[29]	KD [29]	$E_{SN\text{-}anion}$ (kJ/mol)	$E_{cation\text{-}O1E}$ (kJ/mol)
[emim]	[Cl]	1	-	$6.33 \cdot 10^{-10}$	-3875	-2391
	[Br]	7	0.02	$2.29 \cdot 10^{-7}$	-3636	-2343
	[I]	74	-	$4.13 \cdot 10^{-5}$	-2428	-2657
[bmim]	[Cl]	3	0.03	$1.75 \cdot 10^{-9}$	-3338	-1727
	[Br]	35	-	$1.75 \cdot 10^{-7}$	-2987	-1695
	[I]	88	-	$5.05 \cdot 10^{-5}$	-2038	-1796

5. CONCLUSIONS

Relative to experimental or Peng-Robinson data, propylene epoxide, and carbonate molecular dynamics simulations slightly underestimate vapor densities, overestimate liquid densities by 150 Kg/m³, and overestimate critical points. Despite these discrepancies, the force fields qualitatively capture density trends, even though reparameterization and force field improvements should be applied for more accurate experimental results replication.

The modifications made to the propylene epoxide force field in combination with butyl cyclopropane to create the hexylene epoxide force field show a significant impact, with hexylene epoxide liquid densities generally closer to Peng-Robinson predictions. Gas densities are underestimated at higher temperatures (500 and 600 K), and liquid densities are underestimated at lower temperatures (200 and 300 K) and overestimated at higher temperatures (500 and 600 K). The critical point is overestimated compared to Peng-Robinson's prediction around 600 K. The 300-500 K range best reproduces densities, aligning with the experimental conditions of the experimental catalytic reference tests. The qualitative correctness of the model supports its continued use and the applicability of the methodology employed to hexylene carbonate.

Ammonium-based ionic liquid's solubility in hexylene epoxide and carbonate is correctly reproduced with the CL&P force field model in terms of crystallization and diffusion capability. [N4444] cation combined with any of the halide anions: [I], [Br] and [Cl] is soluble in the carbonate/epoxide medium after long simulation times. [N2222] cation in combination with the halides results in the crystallization of the ionic liquids as independent pure phases, therefore being insoluble. Diffused cations and anions are closely interacting and in a similar proportion. This has led to propose that cations define solubility and that the strong cation-anion interactions result in the formation of ion pairs or aggregates rather than dissociated free ions through the reactive media.

For [N4444], [emim] and [bmim] cations combined independently with the three halide anions [I], [Br] and [Cl], cation-anion interaction is the most predominant in the reaction media rather than ions interaction with the reactive carbon or the oxygen in hexylene epoxide. Cation-anion interaction energy followed the trend: [Cl]>[Br]>[I] for fixed cations, which leads to propose that greater cation-anion interaction energies imply a reduction of the ionic liquid catalytic activity. Additionally, [I] anion-based ionic liquids

displayed a slightly more correlated interaction between the cations and the hexylene epoxide Oxygen, which is hypothesized to enable epoxide activation and reaction intermediates stabilization.

MD results describe a stronger cation-anion interaction for [emim] and [bmim] imidazolium-based ionic liquids than [N4444] ammonium-based ionic liquids, in good agreement with the lower reaction media solubility and catalytic activity of the former described by experimental measurements.

6. WORK DIFFUSION

Preliminary results of this work have been exposed as two oral communications:

- **VI Encuentro de Jóvenes Investigadores de la SECAT**, celebrated in Madrid. 12-14 of June 2024.

- **IX Workshop de la Red de Simulación Molecular (RdSiMol)**, celebrated in Baiona (Pontevedra). 16-18 of June 2024.

7. ACKNOWLEDGEMENTS

I want to give special thanks to my girlfriend Cleo, for supporting me at all times and listening again and again to the achievements and errors through which the work has been carried out day by day. This work would be impossible without a constant company capable of giving life a meaning beyond work and oneself. We are the best team. Also, to my mother and sister, for always having words of encouragement to help me stay on the path that one day I decided to take, trusting me every day since then and lighting the way in the darkest nights. Of course, I also want to thank my colleagues in the research group for their participation and especially to Pepe and Pablo, who have provided an ideal starting point from which to advance our knowledge through new techniques for them and some months ago to me. Finally, I wanted to thank Felipe for placing his trust without knowing me and helping me develop a work that a few months ago seemed impossible. Just like Jesus, whose advice and optimism helped to overcome many barriers that raised along the way.

8. BIBLIOGRAPHY

[1] US Department of Commerce, N. *Global Monitoring Laboratory - Carbon Cycle Greenhouse Gases*. https://gml.noaa.gov/ccgg/trends/ (accessed 2024-04-23).

[2] Change, N. G. C. *Global Surface Temperature | NASA Global Climate Change*. Climate Change: Vital Signs of the Planet. https://climate.nasa.gov/vital-signs/global-temperature?intent=121 (accessed 2024-04-23).

[3] GSFC. 2021. Global Mean Sea Level Trend from Integrated Multi-Mission Ocean Altimeters TOPEX/Poseidon, Jason-1, OSTM/Jason-2, and Jason-3 Version 5.1. Ver. 5.1 PO.DAAC, CA, USA. Dataset accessed [2024-06-25] at https://doi.org/10.5067/GMSLM-TJ151.

[4] *IPCC, 2023: Climate Change 2023: Synthesis Report, Summary for Policymakers. Contribution of Working Groups I, II and III to the Sixth Assessment Report of the Intergovernmental Panel on Climate Change [Core Writing Team, H. Lee and J. Romero (eds.)]. IPCC, Geneva, Switzerland.* https://doi.org/10.59327/IPCC/AR6-9789291691647.001 (accessed 2024-04-23)

[5] *Net Zero by 2050 – Analysis*. IEA. https://www.iea.org/reports/net-zero-by-2050 (accessed 2024-04-23)

[6] IEA, Paris, "Tracking Clean Energy Progress 2023," 2023.

[7] IEA, Paris, "CCUS Projects Explorer," 2024

[8] Marcolongo, D. M., Aresta, M., & Dibenedetto, A. (2021). Stepping toward the carbon circular economy (CCE): Integration of solar chemistry and biosystems for an effective CO2 conversion into added value chemicals and fuels. In *Advances in Inorganic Chemistry* (Vol. 78, pp. 289-351). Academic Press.

[9] Pescarmona, P. P., & Taherimehr, M. (2012). Challenges in the catalytic synthesis of cyclic and polymeric carbonates from epoxides and CO 2. *Catalysis Science & Technology*, *2*(11), 2169-2187.

[10] Kamphuis, A. J., Picchioni, F., & Pescarmona, P. P. (2019). CO 2-fixation into cyclic and polymeric carbonates: principles and applications. *Green chemistry*, *21*(3), 406-448.

[11] Sakakura, T., Choi, J. C., & Yasuda, H. (2007). Transformation of carbon dioxide. *Chemical reviews*, *107*(6), 2365-2387.

[12] Su, C. C., He, M., Amine, R., Chen, Z., Sahore, R., Rago, N. D., & Amine, K. (2019). Cyclic carbonate for highly stable cycling of high voltage lithium metal batteries. *Energy Storage Materials*, *17*, 284-292.

[13] Pescarmona, P. P. (2021). Cyclic carbonates synthesised from CO2: Applications, challenges and recent research trends. *Current Opinion in Green and Sustainable Chemistry*, *29*, 100457.

[14] North, M., Pasquale, R., & Young, C. (2010). Synthesis of cyclic carbonates from epoxides and CO 2. *Green Chemistry*, *12*(9), 1514-1539.

[15] Yu, W., Maynard, E., Chiaradia, V., Arno, M. C., & Dove, A. P. (2021). Aliphatic polycarbonates from cyclic carbonate monomers and their application as biomaterials. *Chemical Reviews*, *121*(18), 10865-10907.

[16] Rasool, M. A., Pescarmona, P. P., & Vankelecom, I. F. (2019). Applicability of organic carbonates as green solvents for membrane preparation. *ACS Sustainable Chemistry & Engineering*, *7*(16), 13774-13785.

[17] Belinchon, A., Hernandez, E., Vázquez, J., Santiago, R., Moya, C., Larriba, M., ... & Palomar, J. (2022). Biocarbonates derived from CO2 and terpenes: molecular design

for aqueous mixture treatment driven by COSMO-RS. *ACS Sustainable Chemistry & Engineering*, *10*(29), 9635-9643.

[18] Rodríguez-Llorente, D., Hernández, E., Gutiérrez-Sánchez, P., Navarro, P., Águeda, V. I., Álvarez-Torrellas, S., ... & Larriba, M. (2023). Extraction of pharmaceuticals from hospital wastewater with eutectic solvents and terpenoids: Computational, experimental, and simulation studies. *Chemical Engineering Journal*, *451*, 138544.

[19] Hernández, E., Santiago, R., Moya, C., Navarro, P., & Palomar, J. (2021). Multiscale evaluation of CO2-derived cyclic carbonates to separate hydrocarbons: Drafting new competitive processes. *Fuel Processing Technology*, *212*, 106639.

[20] Ayuso, M., Mateo, S., Belinchón, A., Navarro, P., Palomar, J., García, J., & Rodríguez, F. (2023). Cyclic carbonates as solvents in the dearomatization of refinery streams: Experimental liquid–liquid equilibria, modelling, and simulation. *Journal of Molecular Liquids*, *380*, 121710.

[21] Alves, M., Grignard, B., Méreau, R., Jerome, C., Tassaing, T., & Detrembleur, C. (2017). Organocatalyzed coupling of carbon dioxide with epoxides for the synthesis of cyclic carbonates: catalyst design and mechanistic studies. *Catalysis Science & Technology*, *7*(13), 2651-2684.

[22] Alassmy, Y. A., & Pescarmona, P. P. (2019). The role of water revisited and enhanced: a sustainable catalytic system for the conversion of CO2 into cyclic carbonates under mild conditions. *ChemSusChem*, *12*(16), 3856-3863.

[23] Moya, C., Sabater, V., Yagüe, G., Larriba, M., & Palomar, J. (2018). CO2 conversion to cyclic carbonates catalyzed by ionic liquids with aprotic heterocyclic anions: DFT calculations and operando FTIR analysis. *Journal of CO2 Utilization*, *28*, 66-72.

[24] Palomar, J., Lemus, J., Navarro, P., Moya, C., Santiago, R., Hospital-Benito, D., & Hernandez, E. (2024). Process simulation and optimization on ionic liquids. *Chemical Reviews*, *124*(4), 1649-1737.

[25] Zeng, S., Zhang, X., Bai, L., Zhang, X., Wang, H., Wang, J., ... & Zhang, S. (2017). Ionic-liquid-based CO2 capture systems: structure, interaction and process. *Chemical reviews*, *117*(14), 9625-9673.

[26] Zanatta, M., García-Verdugo, E., & Sans, V. (2023). Direct air capture and integrated conversion of carbon dioxide into cyclic carbonates with basic organic salts. *ACS Sustainable Chemistry & Engineering*, *11*(26), 9613-9619.

[27] Chen, Y., & Mu, T. (2019). Conversion of CO 2 to value-added products mediated by ionic liquids. *Green chemistry*, *21*(10), 2544-2574.

[28] Li, J., Dong, S., An, B., Zhang, Z., Li, Y., Wang, L., & Zhang, J. (2023). Machine learning for the yield prediction of CO2 cyclization reaction catalyzed by the ionic liquids. *Fuel*, *335*, 126942.

[29] E. Hernández, P. Navarro, P.P. Pescarmona, J. Palomar (2024) The role of dissociation on the catalytic activity of organic halides in CO2 Conversion to Cyclic Carbonates: an experimental and computational study.

[30] Bobbink, F. D., Vasilyev, D., Hulla, M., Chamam, S., Menoud, F., Laurenczy, G., ... & Dyson, P. J. (2018). Intricacies of cation–anion combinations in imidazolium salt-catalyzed cycloaddition of CO2 into epoxides. *ACS Catalysis*, *8*(3), 2589-2594.

[31] Butera, V. (2023). Carbon Dioxide Cycloaddition to Epoxides Promoted by Nicotinamidium Halide Catalysts: A DFT Investigation. *ChemPlusChem*, *88*(7), e202300183.

[32] Yan, R., Chen, K., Li, Z., Qu, Y., Gao, L., Tong, H., ... & Guo, K. (2021). Fixation of CO2 into cyclic carbonates by halogen-bonding catalysis. *ChemSusChem*, *14*(2), 738-744.

[33] Xia, Y., Zhang, Y., Su, Q., & Dong, K. (2020). Theoretical insights into the effect of cations, anions, and water on fixation of CO2 catalyzed by different ionic liquids. *ChemSusChem*, *13*(23), 6391-6400.

[34] Della Monica, F., Buonerba, A., Grassi, A., Capacchione, C., & Milione, S. (2016). Glycidol: an hydroxyl-containing epoxide playing the double role of substrate and catalyst for CO2 cycloaddition reactions. *ChemSusChem*, *9*(24), 3457-3464.

[35] Sun, H., & Zhang, D. (2007). Density functional theory study on the cycloaddition of carbon dioxide with propylene oxide catalyzed by alkylmethylimidazolium chlorine ionic liquids. *The Journal of Physical Chemistry A*, *111*(32), 8036-8043.

[36] Yan, R., Chen, K., Li, Z., Qu, Y., Gao, L., Tong, H., ... & Guo, K. (2021). Fixation of CO2 into cyclic carbonates by halogen-bonding catalysis. *ChemSusChem*, *14*(2), 738-744.

[37] Anthofer, M. H., Wilhelm, M. E., Cokoja, M., Markovits, I. I., Pöthig, A., Mink, J., ... & Kühn, F. E. (2014). Cycloaddition of CO 2 and epoxides catalyzed by imidazolium bromides under mild conditions: influence of the cation on catalyst activity. *Catalysis Science & Technology*, *4*(6), 1749-1758.

[38] Cheng, W.; Xiao, B.; Sun, J.; Dong, K.; Zhang, P.; Zhang, S.; Ng, F. T. T. Effect of hydrogen bond of hydroxyl-functionalized ammonium ionic liquids on cycloaddition of CO2. Tetrahedron Letters 2015, 56, 1416.

[39] Cheng, W., Xiao, B., Sun, J., Dong, K., Zhang, P., Zhang, S., & Ng, F. T. (2015). Effect of hydrogen bond of hydroxyl-functionalized ammonium ionic liquids on cycloaddition of CO2. *Tetrahedron Letters*, *56*(11), 1416-1419.

[40] Wang, J. Q., Sun, J., Cheng, W. G., Dong, K., Zhang, X. P., & Zhang, S. J. (2012). Experimental and theoretical studies on hydrogen bond-promoted fixation of carbon dioxide and epoxides in cyclic carbonates. *Physical Chemistry Chemical Physics*, *14*(31), 11021-11026.

[41] Sun, J., Ren, J., Zhang, S., & Cheng, W. (2009). Water as an efficient medium for the synthesis of cyclic carbonate. *Tetrahedron Letters*, *50*(4), 423-426.

[42] Xiao, L., Su, D., Yue, C., & Wu, W. (2014). Protic ionic liquids: A highly efficient catalyst for synthesis of cyclic carbonate from carbon dioxide and epoxides. *Journal of CO2 Utilization*, *6*, 1-6.

[43] Lancaster, N. L., & Welton, T. (2004). Nucleophilicity in ionic liquids. 3.1 anion effects on halide nucleophilicity in a series of 1-Butyl-3-methylimidazolium ionic liquids. *The Journal of Organic Chemistry*, *69*(18), 5986-5992.

[44] Sun, J., Fujita, S. I., Zhao, F., & Arai, M. (2004). Synthesis of styrene carbonate from styrene oxide and carbon dioxide in the presence of zinc bromide and ionic liquid under mild conditions. *Green Chemistry*, *6*(12), 613-616.

[45] Lee, E. H., Ahn, J. Y., Dharman, M. M., Park, D. W., Park, S. W., & Kim, I. (2008). Synthesis of cyclic carbonate from vinyl cyclohexene oxide and CO2 using ionic liquids as catalysts. *Catalysis Today*, *131*(1-4), 130-134.

[46] Kawanami, H., Sasaki, A., Matsui, K., & Ikushima, Y. (2003). A rapid and effective synthesis of propylene carbonate using a supercritical CO 2–ionic liquid system. *Chemical Communications*, (7), 896-897.

[47] Chen, J., Chiarioni, G., Euverink, G. J. W., & Pescarmona, P. P. (2023). Dyes as efficient and reusable organocatalysts for the synthesis of cyclic carbonates from epoxides and CO 2. *Green Chemistry*, *25*(23), 9744-9759.

[48] Marmitt, S., & Goncalves, P. F. (2015). A DFT study on the insertion of CO 2 into styrene oxide catalyzed by 1-butyl-3-methyl-Imidazolium bromide ionic liquid. *Journal of Computational Chemistry*, *36*(17), 1322-1333.

[49] Sun, W., Wang, M., Zhang, Y., Ding, W., Huo, F., Wei, L., & He, H. (2020). Protic vs aprotic ionic liquid for CO2 fixation: A simulation study. *Green Energy & Environment*, *5*(2), 183-194.

[50] Lee, B. S., & Lin, S. T. (2015). A priori prediction of dissociation phenomena and phase behaviors of ionic liquids. *Industrial & Engineering Chemistry Research*, *54*(36), 9005-9012.

[51] Malde, A. K., Zuo, L., Breeze, M., Stroet, M., Poger, D., Nair, P. C., ... & Mark, A. E. (2011). An automated force field topology builder (ATB) and repository: version 1.0. *Journal of chemical theory and computation*, *7*(12), 4026-4037.

[52] Stroet, M., Caron, B., Visscher, K. M., Geerke, D. P., Malde, A. K., & Mark, A. E. (2018). Automated topology builder version 3.0: Prediction of solvation free enthalpies in water and hexane. *Journal of chemical theory and computation*, *14*(11), 5834-5845.

[53] Bernardes, C. E., & Canongia Lopes, J. N. (2017). Modeling halogen bonds in ionic liquids: a force field for imidazolium and halo-imidazolium derivatives. *Journal of Chemical Theory and Computation*, *13*(12), 6167-6176.

[54] Canongia Lopes, J. N., & Pádua, A. A. (2012). CL&P: A generic and systematic force field for ionic liquids modeling. *Theoretical Chemistry Accounts*, *131*, 1-11.

[55] Rutenberg, O. L., & Shakhova, S. F. (1973). The pVT relation on the boundary curve for epoxypropane. *Russ. J. Phys. Chem*, *47*, 124-125.

[56] Kobe, K. A., Ravicz, A. E., & Vohra, S. P. (1956). Critical Properties and Vapor Pressures of Some Ethers and Heterocyclic Compounds. *Industrial & Engineering Chemistry Chemical & Engineering Data Series*, *1*(1), 50-56.

[57] Gurevich, I. G., Gisina, K. B., Shchitnikov, V. K., Dubasova, V. S., & Nikonov, V. L. (1982). Viscosity and density of aprotonic solvents and electrolytes based on them. *Journal of engineering physics*, *42*, 304-308.

[58] Hong, C. S., Wakslak, R., Finston, H., & Fried, V. (1982). Some thermodynamic properties of systems containing propylene carbonate and ethylene carbonate. *Journal of Chemical and Engineering Data*, *27*(2), 146-148.

[59] ThermoData Engine (TDE): Software Implementation of the Dynamic Data Evaluation Concept. 2. Equations of State on Demand and Dynamic Updates over the Web, J. Chem. Inf. Model., 47, 1713-1754, 2007.